Observational evidence of increasing global radiative forcing

Ryan Kramer[1], Haozhe He[2], Brian Soden[2], Lazaros Oreopoulos[1], Gunnar Myhre[3], Piers Forster[4], and Christopher Smith[4]

[1]NASA Goddard Space Flight Center
[2]University of Miami
[3]CICERO Center for International Climate and Environmental Research
[4]University of Leeds

November 22, 2022

Abstract

Changes in atmospheric composition, such as increasing greenhouse gases, cause an initial radiative imbalance to the climate system, quantified as the instantaneous radiative forcing. This fundamental metric has not been directly observed globally and previous estimates have come from models. In part, this is because current space-based instruments cannot distinguish the instantaneous radiative forcing from the climate's radiative response. We apply radiative kernels to satellite observations to disentangle these components and find all-sky instantaneous radiative forcing has increased 0.53±0.11 W/m2 from 2003 through 2018, accounting for positive trends in the total planetary radiative imbalance. This increase has been due to a combination of rising concentrations of well-mixed greenhouse gases and recent reductions in aerosol emissions. These results highlight distinct fingerprints of anthropogenic activity in Earth's changing energy budget, which we find observations can detect within 4 years.

Observational evidence of increasing global radiative forcing

Ryan J. Kramer[1,2,*], Haozhe He[3], Brian J. Soden[3], Lazaros Oreopoulos[1], Gunnar Myhre[4], Piers M. Forster[5], Christopher J. Smith[5,6]

[1]Earth Sciences Division, NASA Goddard Space Flight Center, Greenbelt, MD 20771, USA
[2]Universities Space Research Association, 7178 Columbia Gateway Drive, Columbia, MD 21046, USA
[3]Rosenstiel School of Marine and Atmospheric Science, University of Miami, 4600 Rickenbacker Causeway, Miami, FL 33149, USA
[4]CICERO Center for International Climate and Environmental Research in Oslo, 0318, Oslo, Norway
[5] School of Earth and Environment, University of Leeds, Leeds, LS2 9JT, UK
[6]International Institute for Applied Systems Analysis (IIASA), Laxenburg, 2351, Austria

Corresponding Author: Ryan J. Kramer (ryan.j.kramer@nasa.gov)

Key Points

- Observed instantaneous radiative forcing has increased, strengthening the top-of-atmosphere radiative imbalance.
- Due to cancellations in longwave and shortwave radiation, the sum of rapid adjustments and radiative feedbacks exhibit an insignificant trend.
- Observed increases in instantaneous radiative forcing are direct evidence of the anthropogenic effects on the Earth's radiative energy budget.

Abstract

Changes in atmospheric composition, such as increasing greenhouse gases, cause an initial radiative imbalance to the climate system, quantified as the instantaneous radiative forcing. This fundamental metric has not been directly observed globally and previous estimates have come from models. In part, this is because current space-based instruments cannot distinguish the instantaneous radiative forcing from the climate's radiative response. We apply radiative kernels to satellite observations to disentangle these components and find all-sky instantaneous radiative forcing has increased 0.53±0.11 W/m^2 from 2003 through 2018, accounting for positive trends in the total planetary radiative imbalance. This increase has been due to a combination of rising concentrations of well-mixed greenhouse gases and recent reductions in aerosol emissions. These results highlight distinct fingerprints of anthropogenic activity in Earth's changing energy budget, which we find observations can detect within 4 years.

Plain Language Summary

Climate change is a response to energy imbalances in the climate system. For example, rising greenhouse gases directly cause an initial imbalance, the radiative forcing, in the planetary radiation budget, and surface temperatures increase in response as the climate attempts to restore balance. The radiative forcing and subsequent radiative feedbacks dictate the amount of warming. While there are well-established observational records of greenhouse gas concentrations and surface temperatures, there is not yet a global measure of the radiative forcing, in part because current satellite observations of Earth's radiation only measure the sum total of radiation changes that occur. We use the radiative kernel technique to isolate radiative

forcing from total radiative changes and find it has increased from 2003 through 2018, accounting for nearly all of the long-term growth in the total top-of-atmosphere radiation imbalance during this period. We confirm that rising greenhouse gas concentrations account for most of the increases in the radiative forcing, along with reductions in reflective aerosols. This serves as direct evidence that anthropogenic activity has affected Earth's energy budget in the recent past.

1. Introduction

The Instantaneous Radiative forcing (IRF) is the initial imbalance of the Earth's top-of-the-atmosphere (TOA) radiative energy budget directly caused by a change in atmospheric composition, such as increasing greenhouse gases (GHGs), or perturbed surface properties, like from land use change. All anthropogenic climate changes are a response to the IRF, including surface temperature change and associated radiative feedbacks (Sherwood et al. 2015). Despite a sound basis in physics and radiative transfer theory, the IRF is hard to directly diagnose from observations. Multiple remote sensing and in-situ instruments observe net radiative fluxes, but these measurements convolve the IRF with radiative responses to the changing atmospheric state. Some studies have diagnosed a more broadly defined "greenhouse effect" by evaluating observations of clear-sky longwave radiation at the surface (Philipona et al. 2004) and TOA (Raghuraman et al. 2019), but this analysis does not separate the IRF from water vapor feedback processes.

Harries et al. (2001) compared outgoing longwave radiation at the TOA from two satellite instruments launched decades apart, attributing emission differences at relevant spectral bands to rising greenhouse gas (GHG) concentrations. However, instrumental uncertainty between the two platforms complicates interpretation (Jiang et al. 2011). Feldman et al. (2015,

2018) used ground observations from the US Department of Energy Atmospheric Radiation Measurement (ARM) program to provide the most observationally-oriented assessment to date of GHG surface radiative forcing, which is proportional to the TOA IRF. However, their analysis was limited to longwave (LW) forcing from CO_2 and CH_4 and was only conducted for two locations. The total IRF has not been directly diagnosed globally from observations.

Well understood radiative transfer theory tightly constraints the GHG component of the IRF. Line-by-line radiative transfer models diagnose it within 1% agreement (Collins et al. 2006; Mlynczak et al. 2016; Pincus et al. 2020). However, these highly accurate calculations are computationally expensive, so analysis is often limited to a few idealized atmospheric profiles. Quantifying the IRF globally and over time relies on more efficient but less accurate parameterized radiative transfer models (Soden et al. 2018), which introduces model bias when applied to observations. Diagnosing the IRF from aerosols with these models suffers from the same pitfalls, plus additional uncertainty associated with aerosol optical properties that are not well-observed (Randles et al. 2013; Stier et al. 2013). While there have been recent efforts to constrain aerosol IRF with observations (Bellouin et al. 2020; Watson-Parris et al. 2020), results are usually not temporally resolved.

Here we circumvent these limitations by applying radiative kernels (Soden et al. 2008) to isolate the IRF from radiative feedbacks and rapid adjustments over time. We demonstrate that the IRF has increased with rising GHG concentrations, accounting for recent, positive trends in the total TOA radiative imbalance. More specifically, we consider this IRF to be largely a consequence of concentration changes after anthropogenic emissions are moderated by natural carbon cycle responses (Friedlingstein et al. 2019).

2. Methods

Variations in the total, all-sky radiative energy balance at the TOA, dR, constrain global surface temperature change and consists of the all-sky instantaneous radiative forcing (IRF) and radiative responses to the IRF:

$$dR = IRF + dR_\lambda \qquad (1),$$

where dR_λ is net radiative changes caused by surface temperature-mediated radiative feedbacks and rapid adjustments from, to first order, temperature (T), water vapor (q), surface albedo (α) and cloud (C) changes (Vial et al. 2013; Sherwood et al. 2015):

$$dR_\lambda = dR_T + dR_q + dR_\alpha + dR_C \qquad (2).$$

For simplicity, we will not decompose these terms further into feedbacks and rapid adjustments since it has no bearing on diagnosing the IRF. We simply refer to these radiative anomalies as radiative responses. We note that dR_λ includes both anthropogenic responses and natural variability (e.g. Trenberth et al. 2015).

The Clouds and Earth's Radiant Energy System (CERES) has provided global TOA energy balance observations since 2000. Here, we diagnose dR using radiative flux anomalies from the CERES Energy Balance and Filled (EBAF) Ed. 4.1 product (Loeb et al. 2018a; Loeb et al. 2019). While no observational product measures the radiative response terms in isolation, they can be diagnosed using radiative kernels combined with observations of the relevant state variable, x (B. Zhang et al. 2019; Bony et al. 2020). An individual, non-cloud radiative response, dR_x, in linear form is:

$$dR_x = \frac{\partial R}{\partial x} dx = K_x dx, \;\; x = T, q, \alpha \qquad (3),$$

where K_x is a radiative kernel representing direct radiative changes from small, standard perturbations in state variable x and dx is the actual temperature (T), water vapor (q) or surface albedo (α) climate response. Under clear-sky (CS) conditions:

$$dR^{CS} = IRF^{CS} + dR_{\lambda}^{CS} \qquad (4),$$

where:

$$dR_{\lambda}^{CS} = dR_T^{CS} + dR_q^{CS} + dR_{\alpha}^{CS} \qquad (5).$$

To diagnose dR_x or $dR^{CS}{}_x$ we use observational-based radiative kernels developed from the CloudSat Fluxes and Heating Rates product 2B-FLXHR-LIDAR (Kramer et al. 2019). Unlike GCM-derived radiative kernels, these kernels are free from model bias in the base state, and thus ideal for diagnosing observed radiation changes. Calculating K_x requires using a radiative transfer model to convert base state perturbations to radiative sensitivities. Therefore, using radiative kernels introduces some radiative-transfer model dependency. We apply the radiative kernels to deseasonalized anomalies of temperature and specific humidity profiles from version 6 Level 3 AIRS retrievals (Aumann et al. 2003) to estimate dR_T and dR_q and to surface albedo anomalies from CERES EBAF surface fluxes (Kato et al. 2018) to estimate dR_{α}. Due to computational expense, radiative kernels, including those used here, are often derived from one year of data. However radiative kernel inter-annual variability is small (Pendergrass et al. 2018; Thorsen et al. 2018), therefore applying radiative kernels to the entire observational record is justified.

In the traditional radiative kernel technique used here, the cloud radiative response (dR_C) is calculated as the change in cloud radiative effects (CRE) corrected for cloud masking (Soden et al, 2008; Kramer et al. 2019):

$$dR_C = dCRE - (dR_T - dR_T^{CS}) - \left(dR_q - dR_q^{CS}\right) - (dR_\alpha - dR_\alpha^{CS}) - (IRF - IRF^{CS}) \quad (6),$$

where CRE is the difference between all-sky and clear-sky radiative fluxes. The cloud masking correction is necessary because CRE includes differences between all-sky and clear-sky non-cloud radiative changes, which are not actual cloud radiative responses (Soden et al. 2004). Here *dCRE* is estimated using the TOA CERES EBAF radiative fluxes. The dR_x terms are diagnosed using all-sky and clear-sky radiative kernels as described above.

The ultimate goal of this study is to derive the IRF from these radiative kernel calculations. Under clear-sky conditions, we simply diagnose IRF^{CS} by rearranging Equation 3, whereby:

$$IRF^{cs} = dR^{cs} - dR_\lambda^{cs} = dR^{cs} - \left(dR_T^{cs} + dR_q^{cs} + dR_\alpha^{cs}\right) \quad (7),$$

For all-sky conditions, an analogous calculation would require dR_C to be removed from dR, but since estimating dR_C as in equation 6 requires the IRF to be known, this differencing technique is not possible. Following common practice (Soden et al. 2008; Vial et al. 2013), we estimate the all-sky IRF as:

$$IRF = \frac{IRF^{CS}}{Cl} \quad (8),$$

where Cl is a constant that accounts for cloud masking of the IRF. For the longwave (LW) Cl, we use a constant of 1.24, derived by dividing clear-sky and all-sky double-call radiative transfer calculations of CO_2 IRF from models (Smith et al. 2018). The cloud mask for the shortwave (SW) is derived from direct output of aerosol IRF from Modern-Era Retrospective Analysis for Research and Applications, Version 2 (MERRA-2) reanalysis (Gelaro et al. 2017). The global-mean value is 2.43, in line with a range of observational-based cloud masking estimates by Bellouin et al. (2020). Only the MERRA-2 SW Cl is available over time, but it has an insignificant long-term trend. Consequently, SW IRF has nearly identical trends when computed with a time resolved versus constant SW Cl.

This conversion to all-sky conditions accounts for the presence of clouds but not cloud changes. Therefore, the IRF in this study does not include aerosol-cloud interactions, such as cloud albedo effects (Boucher et al. 2013). Instead, these terms are included in dR_C. Therefore, the aerosol component to the kernel-derived estimates of IRF is akin to aerosol direct radiative effects found throughout the literature (e.g. Thorsen et al. 2020).

The AIRS L3 data has the shortest record among satellite observations used in this study, with 2003 being the first complete year of data. Thus, we compute all deseasonalized anomalies from 2003 through 2018 relative to the mean of that time span. While we refer to the resulting calculation as the IRF for brevity, we actually show anomalies of the IRF. For comparison, we also estimate the IRF by applying the CloudSat radiative kernels to MERRA-2 reanalysis over the same period. This reanalysis product assimilates a variety of satellite observations, including observations of aerosol properties.

In climate models, idealized simulations and flux diagnostics from double-call radiative transfer calculations can be used to evaluate the accuracy of radiative kernel estimates of dR_{λ} and IRF (e.g. Vial et al. 2013; Smith et al. 2018). Such a comparison is not possible in the observed record or the MERRA-2 reanalysis, however. Since the IRF is derived from differencing the other radiative terms, there will always be near-perfect energy closure, albeit with some error due to cloud masking assumptions, which is typically small (Chung and Soden 2015). Alternatively, we will compare these kernel-derived estimates to various independent measures of the IRF.

To verify the aerosol component of the IRF, we compare radiative kernel-derived SW IRF to direct output of the aerosol direct radiative effect from MERRA-2. We also compare SW IRF to trends in aerosol optical depth (AOD) from MERRA-2 and observations from the Moderate Resolution Imaging Spectroradiometer (MODIS) merged Dark Target and Deep Blue product (Sayer et al. 2014).

We compare radiative-kernel derived estimates of the LW IRF to offline radiative transfer calculations of GHG IRF. We apply empirical formulas to observed global-mean concentrations of 5 major greenhouse gases (CO_2, CH_4, N_2O, CFC-11 and CFC-12), provided by NOAA Global Monitoring Division (Hoffman et al. 2006; Montzka et al. 2011). Etminan et al. (2016) derive the empirical formulas from polynomial fits to line-by-line radiative forcing calculations. While these formulas were originally developed for net stratospherically adjusted radiative forcing, we use corrections from additional line-by-line calculations (Hodnebrog et al. 2013; Etminan et al. 2016) to calculate TOA IRF, decomposed into a LW and SW component.

We also estimate GHG IRF using the SOCRATES offline radiative transfer model (Edwards et al. 1996; Manners et al. 2015) with NOAA GHG concentrations and atmospheric profiles from the MERRA-2 reanalysis. Like the other IRF estimates, these calculations are presented in anomaly space with the seasonal cycle removed. The IRF from CFCs has decreased recently, but this has been compensated for by a near equal increase from other halocarbons not considered in empirical fit and SOCRATES calculations (Myhre et al. 2013a). To account for this, we repeat these calculations with no CFC trend. This only modifies total GHG IRF trends by <5%, however, so hereafter we focus on results without this assumption. The SOCRATES IRF calculations are conducted under pristine, clear-sky conditions and converted to all-sky via Equation 8, like the radiative kernel calculations.

The various inputs and assumptions detailed above can contribute uncertainty to the estimated radiative changes. In a Supplemental Appendix we provide a comprehensive uncertainty assessment in the IRF trends due to these contributors, including from observed dR, radiative kernels, and the cloud masking constant, Cl. We find these uncertainties are smaller than the trend regression uncertainty associated with timeseries variability. Therefore, all trends presented hereafter are provided with 95% confidence intervals (or roughly 2 standard errors around the mean) associated with the least-squares linear regression. This is common practice when diagnosing CERES trends (e.g. Loeb et al. 2018a,b).

The anomalies of dR, dR_λ and the IRF are subject to the same sources of uncertainty as long-term trends. Therefore, Figure 1 and 2 below include uncertainty bounds diagnosed as 2σ across multiple estimates of the radiative terms using different radiative flux data products from CERES and alternative radiative kernel sets and model estimates of Cl (see Supplemental Appendix).

3. Results

Figure 1a shows a timeseries of global-mean total radiative flux anomalies (dR) from CERES satellite observations and its component from radiative responses (dR_λ), estimated by applying the CloudSat-based radiative kernels to CERES and AIRS observations (hereafter CERES/AIRS). Positive anomalies indicate a net increase in downwelling radiation at the TOA (planetary warming). The sum of the radiative responses, dR_{λ}, accounts for nearly all of the total short-term dR variability, as evident by their strong correlation (r=0.88) and small root-mean-squared difference of 0.024±0.003 W/m^2; ~3.5% of the standard deviation of dR. On inter-annual timescales, ENSO strongly influences this variability (Trenberth et al. 2014), which lags by ~5 months (Supplemental Fig. S1; Loeb et al. 2018b). Long-term dR exhibits a positive, linear trend (0.038±0.02 W/m^2/year) significant with 95% confidence, while dR_{λ} exhibits an insignificant trend (0.002±0.02 W/m^2/year) an order of magnitude smaller. This arises from cancelation between LW and SW dR_{λ}. The LW dR_{λ} has a negative linear trend (-0.042±0.02 W/m^2/year) (Fig. 1b), mainly from global warming-driven dR_T decreases (-0.041±0.007 W/m^2/year) (Supplemental Fig. S2). The SW dR_{λ} trend (0.044±0.02 W/m^2/year) is nearly equal and opposite of the LW, driven by increases in SW dR_{α} (0.023±0.09 W/m^2/year) and SW dR_C (0.020±0.13 W/m^2/year), a predominantly low cloud response (Loeb et al. 2018b). The latter alone accounts for most of the SW interannual variability.

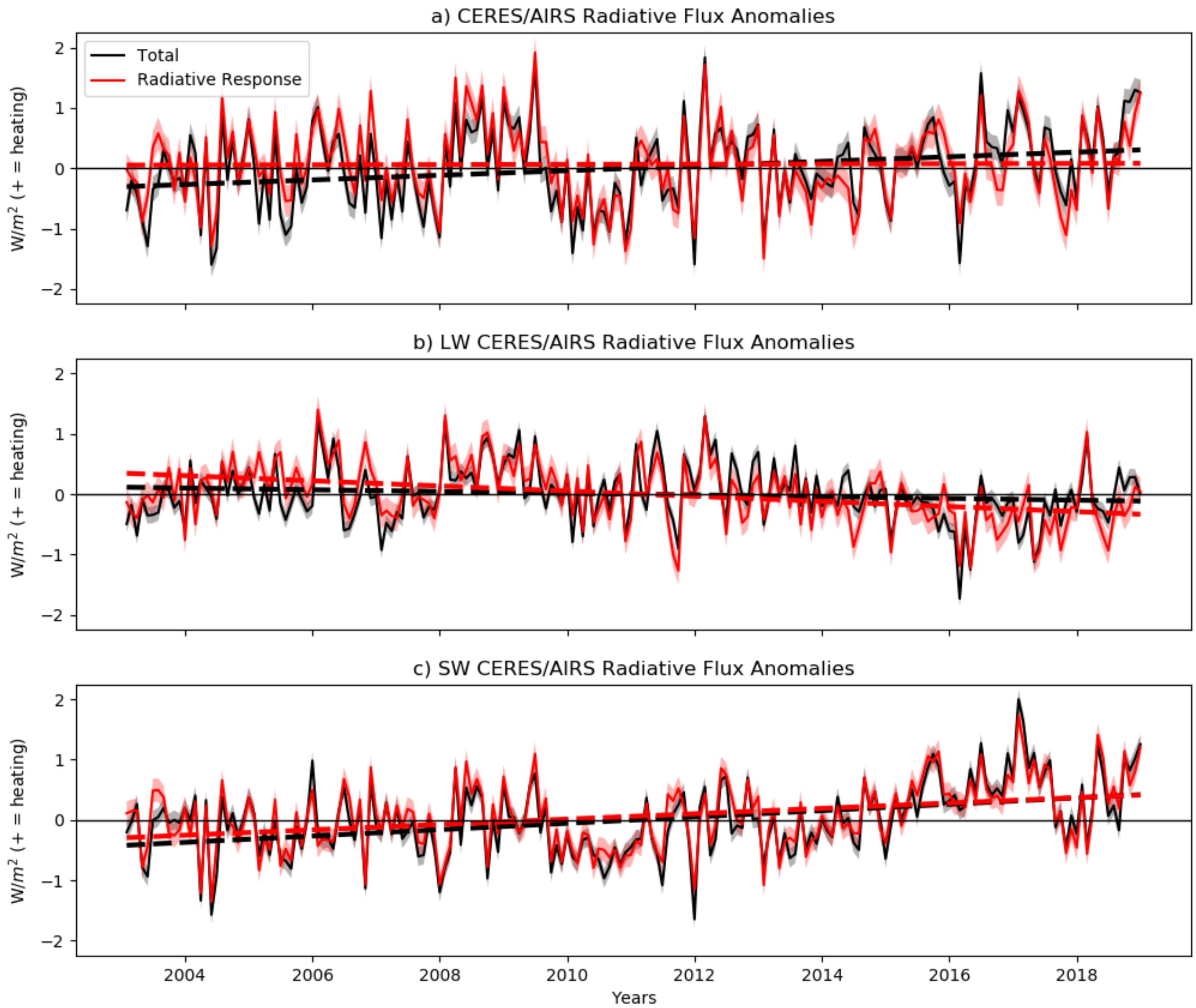

Figure 1. *Global-mean a) net, b) longwave (LW) and c) shortwave (SW) total radiative flux anomalies from 2003 through 2018 as measured by CERES (black) and the contribution to that total from the sum of radiative responses (red). Respective trendlines are displayed as dashed lines. Uncertainty of +/-2σ is shown for each timeseries, computed as described in the Methods. Linear trends and 95% confidence intervals are provided in text.*

MERRA-2 also exhibits a significant, positive trend in dR but not dR_λ due to compensating LW and SW components (Supplemental Fig. S3). However, there is a positive trend in LW dR_λ and a negative trend in SW dR_λ, opposite from the CERES/AIRS response. This occurs due to a considerably different LW and SW dR_C (Supplemental Fig. S4) compared to satellite observations.

Since neither dR_λ or its uncertainties account for the positive dR trend, it must be explained by the IRF. Figure 2 shows the timeseries of the total, LW and SW IRF under all-sky conditions, estimated from the radiative kernel technique. The total CERES/AIRS IRF exhibits a significant, positive trend (0.033±0.007 W/m^2/year), mostly from increasing LW IRF (0.027±0.006 W/m^2/year). The SW IRF exhibits a smaller, yet still significant increase (0.006±0.003 W/m^2/year). The LW IRF trend is opposite in sign from LW dR, since decreasing LW dR_λ compensates. In the SW, IRF and dR are both increasing, but SW dR_λ is the dominant contributor while the IRF trend is much smaller.

Rising GHG concentrations explain the positive LW IRF trend. Accordingly, it increases at a similar rate to the GHG IRF estimates from the empirical fit (0.021±0.0002 W/m^2/year or 0.022±0.0002 W/m^2/year if ignoring CFCs [see Methods]) and the SOCRATES radiative transfer model (0.023±0.0003 W/m^2/year) (Fig. 2b), despite these calculations neglecting some GHG forcers found in nature, such as ozone. MERRA-2 exhibits a similar LW IRF trend to CERES/AIRS (0.029±0.003 W/m^2/year) while direct output of the LW aerosol IRF from MERRA-2 exhibits no trend. This further indicates GHG increases account for roughly all LW IRF increases.

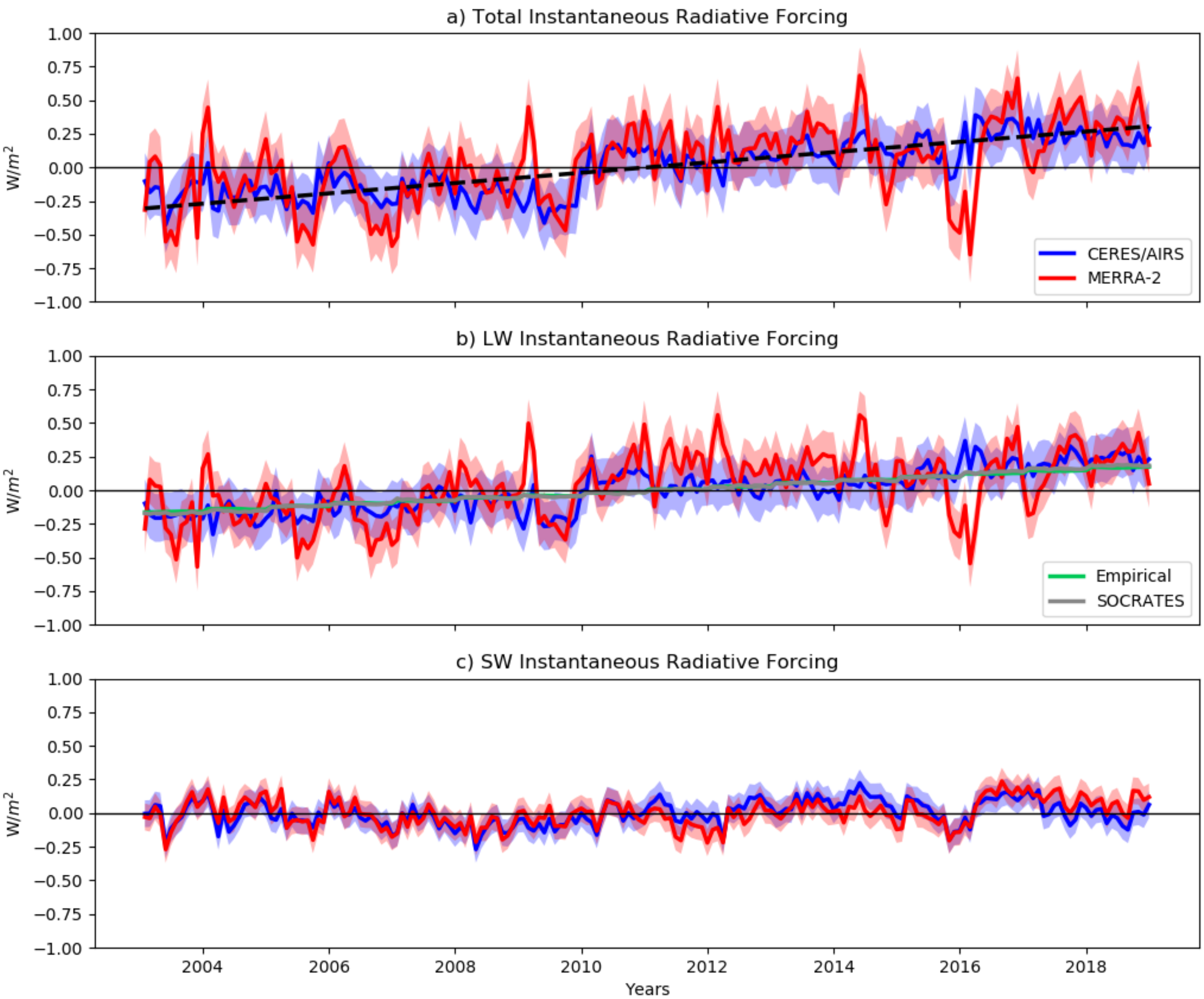

Figure 2. *Global-mean a) total, b) longwave (LW) and c) shortwave (SW) instantaneous radiative forcing (IRF) estimated from the radiative kernel technique for CERES/AIRS (red) and MERRA-2 (blue). Additional calculations of greenhouse gas-only IRF are also shown using empirical formulas (green) and the SOCRATES radiative transfer model (gray). For reference, the trendline for total radiative flux anomalies (Fig 1a) is displayed with the total IRF as a black dashed line. Uncertainty of +/-2σ is shown with shading for each timeseries, computed as described in the Methods. Linear trends and 95% confidence intervals are provided in text and in Table 1.*

Increasing GHG concentrations also contribute (0.002±0.00 W/m^2/year) to the total positive SW IRF trends, according to estimates from the empirical fits. The SW GHG trend is negligible in the SOCRATES calculations, but the model version used here does not account for the SW absorption of CH_4.

The total SW IRF increase is nearly identical in CERES/AIRS and MERRA-2, and to aerosol-only SW IRF trends from MERRA-2 direct output (Supplemental Fig. S5). They also exhibit similar short-term variability. This suggests aerosols explain most of the SW IRF. The long-term radiative heating is consistent with declining anthropogenic aerosol emissions during this period (Q. Zhang et al. 2019). Towards the end of the timeseries, CERES/AIRS SW IRF has more positive anomalies. Locally, the largest differences with MERRA-2 after 2015 are in major absorbing aerosol source regions (Supplemental Fig. S6), suggesting a contribution from different absorbing aerosol properties.

Figure 3 shows local linear trends in kernel-derived, total SW IRF from CERES/AIRS and MERRA-2 and direct MERRA-2 output of aerosol-only SW IRF (Figure 3c). The spatial pattern of the SW IRF trend is generally consistent across all three estimates. A notable hemispheric asymmetry is present, with large changes concentrated in the populous Northern Hemisphere. This includes large positive trends over the Eastern United States, Western Europe and Eastern China, where anthropogenic emissions of reflective aerosols have declined because of government actions to combat poor air quality (Kühn et al. 2014; Ridley et al. 2018; Q. Zhang et al. 2019). In contrast, the SW IRF trends are negative over India, where emissions continue to rise (Dey et al. 2012).

There are some magnitude differences in these major source regions, however. For instance, trends are larger in the Eastern US and India in CERES/AIRS than in MERRA-2. This coincides with differences in the MODIS and MERRA-2 AOD trends (Figure 3d,e), which are also larger in CERES/AIRS. Over Saharan Africa, the sign of the SW IRF trend differs, consistent with opposing trends in MODIS and MERRA-2 AOD. Dust radiative forcing during this period is likely a key factor (Supplemental Fig. S7; Shao et al. 2013) and is highly uncertain (Miller et al. 2014; Kok et al. 2017).

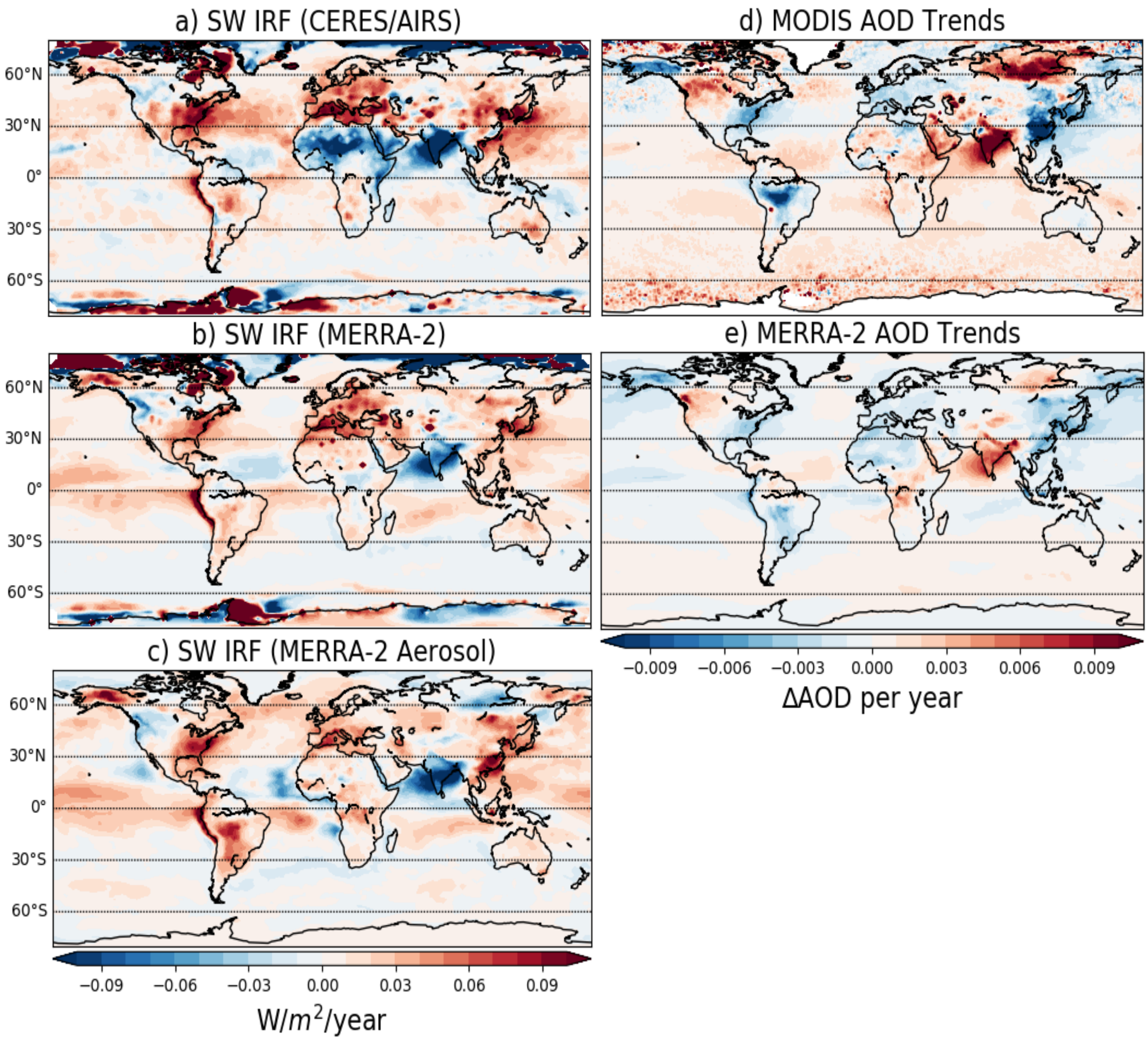

Figure 3. *Local linear trends from 2003 through 2018 in all-sky shortwave instantaneous radiative forcing (SW IRF) diagnosed in a) CERES/AIRS observations and b) MERRA-2 reanalysis using the radiative kernel differencing technique and c) from direct output of MERRA-2 aerosol IRF. Also, local linear trends over the same time period are shown for aerosol optical depth (AOD) from d) MODIS and e) MERRA-2.*

The strong agreement in MERRA-2 trends from kernel differencing versus direct SW aerosol IRF output (Fig 3b,c) highlights the dominant role of aerosols in the total SW IRF trends. It also confirms the accuracy of the radiative kernel technique. The kernel differencing method results in artifacts in the polar regions, however, where large local trends are a consequence of underestimating the SW dR_α removed from dR (Supplemental Fig. S8) and not from actual forcing. One possible explanation is surface albedo radiative kernels fail to capture important ice-albedo feedback non-linearities (Block and Mauritsen 2013). Nevertheless, the polar region errors have negligible effect on global-mean SW IRF trends.

Some inter- and intra-annual variability (hereafter short-term variability) in SW IRF is expected, given natural variations in aerosol concentrations. Consequently, the detrended aerosol-only (σ=0.088 W/m^2) and kernel-derived (σ=0.097 W/m^2) SW IRF in MERRA-2 exhibit similar variability and are highly correlated (r=0.78). The source of the notable short-term variability in LW IRF (Fig. 2b) is less apparent, however, since greenhouse gas concentrations increase relatively steadily on these timescales, as evident in the empirical fit estimate of GHG IRF, which increases almost perfectly linearly.

While radiative kernel error may play some role, the LW IRF from CERES/AIRS exhibits considerably more short-term variability (σ=0.24) than MERRA-2 (σ=0.16), despite using the same CloudSat-derived radiative kernels in both estimates. This highlights short-term inconsistencies between the radiative fluxes observed by CERES (dR^{cs}) and the AIRS retrievals used to diagnose LW dR_λ^{cs}. For instance, the difference between CERES/AIRS and MERRA-2 dR_λ^{cs} exhibits considerably more short-term variability than the difference between dR^{cs}. This is mostly due to different variability in dR_T^{cs} (Supplemental Fig. S9), and more specifically due to different temperature anomalies at the surface and in the boundary layer between AIRS and MERRA-2 (Supplemental Fig. S10). Since AIRS temperature anomalies are more variable, so is the dR_T^{cs} estimate. And since this variability is not also observed radiatively by CERES, it is not evident in dR^{cs}. This ultimately translates to a more variable LW IRF when using the kernel differencing technique. This also explains why LW IRF spatial patterns are noisier for CERES/AIRS than for MERRA-2 (Supplemental Fig. S11). Cloud contamination likely contributes to the AIRS temperature variability, as found previously (Hearty et al. 2014). This is evident at the surface, for example, where the largest differences between AIRS and MERRA-2 temperature anomalies tend to occur where clouds are common (Supplemental Fig. S9), especially over land. While global-mean surface temperature anomalies from AIRS closely agree with other, independent datasets (Susskind et al. 2019), it is possible the temperature biases that do exist are magnified in the context of radiative changes.

The LW IRF variability may also stem from its sensitivity to the atmospheric base state (Pincus et al. 2015). However, this contribution appears to be small. In the LW GHG IRF estimated from the SOCRATES radiative transfer model, we use daily MERRA-2 temperature, surface albedo and humidity data, thus capturing the GHG IRF sensitivity to the unperturbed, non-cloud base state. Still, the short-term variability from this offline calculation is nearly as small as estimates with the empirical fit, which does not account for base state variability. The LW IRF short-term variability in this comparison (and in the radiative kernel-derived estimates) is not due to variations in the cloud base state since LW cloud masking is always treated as a constant. While clouds may play a greater role in reality, the SW IRF estimated from radiative kernels with constant cloud masking has similar short-term variability to the aerosol-only SW IRF in MERRA-2, which accounts for cloud masking temporal variations. This suggests cloud variability may not be important in the global-mean. Lastly, some LW IRF variability in MERRA-2 (and in CERES/AIRS) may be due to spatial variability in the GHG concentrations (Myhre et al. 2013a), which is not present in the empirical fit or the SOCRATES estimates.

	LW	**SW**	**Net**
CERES/AIRS	0.027±0.006	0.006±0.003	0.033±0.007
MERRA-2	0.029±0.003	0.006±0.003	0.035±0.004
Aerosol-Only MERRA-2	-4.2E-4±1.5E-4	0.006±0.003	0.006±0.003

Table 1. *Global-mean linear trends (W/m^2/year) and 95% confidence bounds in instantaneous radiative forcing estimated using the radiative kernel differencing technique (first two rows) and MERRA-2 flux diagnostics (third row).*

4. Conclusions

We have diagnosed the global instantaneous radiative forcing (IRF) directly from observations using radiative kernels. Table 1 summarizes linear trends. We find that from 2003 through 2018, the observed IRF has increased 0.53±0.11 W/m^2, almost entirely accounting for the positive trend in CERES Top-of-Atmosphere (TOA) radiative flux anomalies (*dR).* The intrinsic LW and SW climate radiative responses largely cancel out. This IRF increase mostly occurs in the LW (0.43±0.1 W/m^2), driven by rising greenhouse gas concentrations. This serves as direct observational evidence that anthropogenic activity is impacting the Earth's energy balance. The SW IRF has also increased (0.1±0.05 W/m^2). In part, this is a reflection of government-mandated aerosol emission reductions throughout major source regions, which may have a greater direct impact than inferred by the SW IRF, which does not include aerosol cloud-albedo effects in this analysis.

Diagnosing the observed IRF is important for our fundamental understanding of Earth's response to climate change and a valuable piece of information for policy decisions. Conceivably, observed IRF could be used as a top-down approach for monitoring the climate response to mitigation efforts. By applying published metrics of instrumental uncertainty in AIRS (Tobin et al. 2006; Hearty et al. 2014) and CERES (Loeb et al. 2018a), along with the kernel-derived IRF variance and trend, we apply formulas by Leroy et al. (2008) to determine the minimum length of the observational record necessary to detect a climate change signal. These formulas account for trend uncertainty due to natural variability and instrumental uncertainty. Using this approach, we find total IRF trends are detectable, given these sources of uncertainty, within 3.8 years using the satellite data presented in this study. Therefore, the methods introduced here could be useful for near-real time monitoring, especially since the time to detection shortens with the lengthening of the observational record.

Acknowledgements: We thank the Editor, reviewers and Graeme Stephens for valuable feedback on this work. RJK is supported by an appointment to the NASA Postdoctoral Program administered by Universities Space Research Association. HH and BJS are supported by NASA award 80NSSC18K1032. LO gratefully acknowledges support from NASA's CloudSat/CALIPSO Science Team and MEaSUREs programs. GM, PMF and CJS were supported by European Union's Horizon 2020 Research and Innovation Programme under grant agreement no. 820829 (CONSTRAIN). PMF and CJS were also supported by UKRI NERC grant NE/N006038/1 (SMURPHS). C.J.S. was supported by a NERC/IIASA Collaborative Research Fellowship (NE/T009381/1).

Competing Interests: Authors have no competing interests.

Data and Materials Availability: The CERES radiative flux observations are available at https://ceres.larc.nasa.gov/data/. The AIRS temperature and water vapor observations and the MERRA-2 reanalysis data are available at https://disc.gsfc.nasa.gov/. The CloudSat/CALIPSO radiative kernels used in this study and related code for applying them are available at https://climate.rsmas.miami.edu/data/radiative-kernels/.

References

Aumann, H.H., Chahine, M.T., Gautier, C.,M. Goldberg, D., Kalnay, E., McMillin, L.M., et al. (2003). AIRS/AMSU/HSB on the Aqua mission: design, science objectives, data products, and processing systems. *IEEE Transactions on Geoscience and Remote Sensing*, *41*(2), 253–264. https://doi.org/10.1109/TGRS.2002.808356

Bellouin, N., Quaas, J., Gryspeerdt, E., Kinne, S., Stier, P., Watson-Parris, D., et al. (2020). Bounding Global Aerosol Radiative Forcing of Climate Change. *Reviews of Geophysics*, *58*(1), e2019RG000660. https://doi.org/10.1029/2019RG000660

Block, K., & Mauritsen, T. (2013). Forcing and feedback in the MPI-ESM-LR coupled model under abruptly quadrupled CO2. *Journal of Advances in Modeling Earth Systems*, *5*(4), 676–691. https://doi.org/10.1002/jame.20041

Bony, S., Semie, A., Kramer, R. J., Soden, B., Tompkins, A. M., & Emanuel, K. A. (2020). Observed Modulation of the Tropical Radiation Budget by Deep Convective Organization and Lower-Tropospheric Stability. *AGU Advances*, *1*(3). https://doi.org/10.1029/2019AV000155

Boucher, O., Randall, D., Artaxo, P., Bretherton, C., Feingold, G., Forster, P., et al., (2013) Clouds and aerosols. In *Climate Change 2013: The Physical Science Basis. Contribution of Working Group I to the Fifth Assessment Report of the Intergovernmental Panel on Climate Change*. T.F. Stocker, D. Qin, G.-K. Plattner, M. Tignor, S.K. Allen, J. Doschung, A. Nauels, Y. Xia, V. Bex, and P.M. Midgley, Eds. Cambridge University Press, pp. 571-657, doi:10.1017/CBO9781107415324.016.

Chung, E.-S., & Soden, B. J. (2015). An Assessment of Direct Radiative Forcing, Radiative Adjustments, and Radiative Feedbacks in Coupled Ocean–Atmosphere Models*. *Journal of Climate*, *28*(10), 4152–4170. https://doi.org/10.1175/JCLI-D-14-00436.1

Collins, W. D., Ramaswamy, V., Schwarzkopf, M. D., Sun, Y., Portmann, R. W., Fu, Q., et al. (2006). Radiative forcing by well-mixed greenhouse gases: Estimates from climate models in the Intergovernmental Panel on Climate Change (IPCC) Fourth Assessment Report (AR4). *Journal of Geophysical Research*, *111*(D14), D14317. https://doi.org/10.1029/2005JD006713

Dey, S., Di Girolamo, L., van Donkelaar, A., Tripathi, S. N., Gupta, T., & Mohan, M. (2012). Variability of outdoor fine particulate (PM2.5) concentration in the Indian Subcontinent: A remote sensing approach. *Remote Sensing of Environment*, *127*, 153–161. https://doi.org/10.1016/j.rse.2012.08.021

Edwards, J. M., & Slingo, A. (1996). Studies with a flexible new radiation code. I: Choosing a configuration for a large-scale model. *Quarterly Journal of the Royal Meteorological Society*, *122*(531), 689–719. https://doi.org/10.1002/qj.49712253107

Etminan, M., Myhre, G., Highwood, E. J., & Shine, K. P. (2016). Radiative forcing of carbon dioxide, methane, and nitrous oxide: A significant revision of the methane radiative forcing. *Geophysical Research Letters*, *43*(24), 12,614-12,623. https://doi.org/10.1002/2016GL071930

Feldman, D. R., Collins, W. D., Gero, P. J., Torn, M. S., Mlawer, E. J., & Shippert, T. R. (2015). Observational determination of surface radiative forcing by CO2 from 2000 to 2010. *Nature*, *519*(7543), 339–343. https://doi.org/10.1038/nature14240

Feldman, D. R., Collins, W. D., Biraud, S. C., Risser, M. D., Turner, D. D., Gero, P. J., et al. (2018). Observationally derived rise in methane surface forcing mediated by water vapour trends. *Nature Geoscience*, *11*(4), 238–243. https://doi.org/10.1038/s41561-018-0085-9

Friedlingstein, P., Jones, M. W., O'Sullivan, M., Andrew, R. M., Hauck, J., Peters, G. P., et al. (2019). Global Carbon Budget 2019. *Earth System Science Data*, *11*(4), 1783–1838. https://doi.org/10.5194/essd-11-1783-2019

Gelaro, R., McCarty, W., Suárez, M. J., Todling, R., Molod, A., Takacs, L., et al. (2017). The Modern-Era Retrospective Analysis for Research and Applications, Version 2 (MERRA-2). *Journal of Climate*, *30*(14), 5419–5454. https://doi.org/10.1175/JCLI-D-16-0758.1

Harries, J. E., Brindley, H. E., Sagoo, P. J., & Bantges, R. J. (2001). Increases in greenhouse forcing inferred from the outgoing longwave radiation spectra of the Earth in 1970 and 1997. *Nature*, *410*(6826), 355–357. https://doi.org/10.1038/35066553

Hearty, T. J., Savtchenko, A., Tian, B., Fetzer, E., Yung, Y. L., Theobald, M., et al. (2014). Estimating sampling biases and measurement uncertainties of AIRS/AMSU-A temperature and water vapor observations using MERRA reanalysis. *Journal of Geophysical Research: Atmospheres*, *119*(6), 2725–2741. https://doi.org/10.1002/2013JD021205

Hodnebrog, Ø., Etminan, M., Fuglestvedt, J. S., Marston, G., Myhre, G., Nielsen, C. J., et al. (2013). Global warming potentials and radiative efficiencies of halocarbons and related compounds: A comprehensive review. *Reviews of Geophysics*, *51*(2), 300–378. https://doi.org/10.1002/rog.20013

Hofmann, D. J., Butler, J. H., Dlugokencky, E. J., Elkins, J. W., Masarie, K., Montzka, S. A., & Tans, P. (2006). The role of carbon dioxide in climate forcing from 1979 to 2004: introduction of the Annual Greenhouse Gas Index. *Tellus B: Chemical and Physical Meteorology*, *58*(5), 614–619. https://doi.org/10.1111/j.1600-0889.2006.00201.x

Jiang, Y., Aumann, H.H., Wingyee-Lau, M., & Yung, Y.L. (2011). Climate change sensitivity evaluation from AIRS and IRIS measurements. *Proc. SPIE* 8153, XVI (2011), doi: http://dx.doi.org/10.1117/12.892817

Kato, S., Rose, F. G., Rutan, D. A., Thorsen, T. J., Loeb, N. G., Doelling, D. R., et al. (2018). Surface Irradiances of Edition 4.0 Clouds and the Earth's Radiant Energy System (CERES) Energy Balanced and Filled (EBAF) Data Product. *Journal of Climate*, *31*(11), 4501–4527. https://doi.org/10.1175/JCLI-D-17-0523.1

Kok, J. F., Ridley, D. A., Zhou, Q., Miller, R. L., Zhao, C., Heald, C. L., et al. (2017). Smaller desert dust cooling effect estimated from analysis of dust size and abundance. *Nature Geoscience*, *10*(4), 274–278. https://doi.org/10.1038/ngeo2912

Kramer, R. J., Matus, A. V., Soden, B. J., & L'Ecuyer, T. S. (2019). Observation-Based Radiative Kernels From CloudSat/CALIPSO. *Journal of Geophysical Research: Atmospheres*, 2018JD029021. https://doi.org/10.1029/2018JD029021

Kühn, T., Partanen, A.-I., Laakso, A., Lu, Z., Bergman, T., Mikkonen, S., et al. (2014). Climate impacts of changing aerosol emissions since 1996. *Geophysical Research Letters*, *41*(13), 4711–4718. https://doi.org/10.1002/2014GL060349

Leroy, S.S., Anderson, J.G., & Ohring, G. (2008) Climate Signal Detection Times and Constraints on Climate Benchmark Accuracy Requirements. *Journal of Climate*. *21*, 841–846

Loeb, N. G., Doelling, D. R., Wang, H., Su, W., Nguyen, C., Corbett, J. G., et al. (2018a). Clouds and the Earth's Radiant Energy System (CERES) Energy Balanced and Filled (EBAF) Top-of-Atmosphere (TOA) Edition-4.0 Data Product. *Journal of Climate*, *31*(2), 895–918. https://doi.org/10.1175/JCLI-D-17-0208.1

Loeb, N., Thorsen, T., Norris, J., Wang, H., & Su, W. (2018b) Changes in Earth's Energy Budget during and after the "Pause" in Global Warming: An Observational Perspective, *Climate* 6, 62.

Loeb, N. G., Rose, F. G., Kato, S., Rutan, D. A., Su, W., Wang, H., et al. (2019). Toward a Consistent Definition between Satellite and Model Clear-Sky Radiative Fluxes. *Journal of Climate*, *33*(1), 61–75. https://doi.org/10.1175/JCLI-D-19-0381.1

Manners J, Edwards JM, Hill P, Thelen J-C. (2015). SOCRATES (Suite Of Community RAdiative Transfer codes based on Edwards and Slingo) Technical Guide. Met Office, UK.

Miller, R. L., Knippertz, P., Pérez García-Pando, C., Perlwitz, J. P., & Tegen, I. (2014). Impact of Dust Radiative Forcing upon Climate. In P. Knippertz & J.-B. W. Stuut (Eds.), *Mineral Dust: A Key Player in the Earth System* (pp. 327–357). Dordrecht: Springer Netherlands. https://doi.org/10.1007/978-94-017-8978-3_13

Mlynczak, M. G., Daniels, T. S., Kratz, D. P., Feldman, D. R., Collins, W. D., Mlawer, E. J., et al. (2016). The spectroscopic foundation of radiative forcing of climate by carbon dioxide. *Geophysical Research Letters*, *43*(10), 5318–5325. https://doi.org/10.1002/2016GL068837

Montzka, S. A., Dlugokencky, E. J., & Butler, J. H. (2011). Non-CO2 greenhouse gases and climate change. *Nature*, *476*(7358), 43–50. https://doi.org/10.1038/nature10322

Myhre, G., Shindell, D., Bréon, F.-M., Collins, W., Fuglestvedt, J., Huang, J., Koch, D., Lamarque, J.-F., Lee, E., et al., (2013a). Anthropogenic and natural radiative forcing. In *Climate Change 2013: The Physical Science Basis. Contribution of Working Group I to the Fifth Assessment Report of the Intergovernmental Panel on Climate Change*. T.F. Stocker, D. Qin, G.-K. Plattner, M. Tignor, S.K. Allen, J. Doschung, A. Nauels, Y. Xia, V. Bex, and P.M. Midgley, Eds. Cambridge University Press, pp. 659-740, doi:10.1017/CBO9781107415324.018

Myhre, G., Samset, B. H., Schulz, M., Balkanski, Y., Bauer, S., Berntsen, T. K., et al. (2013b). Radiative forcing of the direct aerosol effect from AeroCom Phase II simulations. *Atmospheric Chemistry and Physics*, *13*(4), 1853–1877. https://doi.org/10.5194/acp-13-1853-2013

Pendergrass, A. G., Conley, A., & Vitt, F. M. (2018). Surface and top-of-atmosphere radiative feedback kernels for CESM-CAM5. *Earth System Science Data*, *10*(1), 317–324. https://doi.org/10.5194/essd-10-317-2018

Philipona, R., Dürr, B., Marty, C., Ohmura, A., & Wild, M. (2004). Radiative forcing - measured at Earth's surface - corroborate the increasing greenhouse effect. *Geophysical Research Letters*, *31*(3). https://doi.org/10.1029/2003GL018765

Pincus, R., Mlawer, E. J., Oreopoulos, L., Ackerman, A. S., Baek, S., Brath, M., et al. (2015). Radiative flux and forcing parameterization error in aerosol-free clear skies. *Geophysical Research Letters*, *42*(13), 5485–5492. https://doi.org/10.1002/2015GL064291

Pincus, R., Buehler, S. A., Brath, M., Jamil, O., Evans, F., Manners, J., et al. (2020). Benchmark calculations of radiative forcing by greenhouse gases. *Earth and Space Science Open Archive*, 15. https://doi.org/10.1002/essoar.10501550.1

Randles, C. A., Kinne, S., Myhre, G., Schulz, M., Stier, P., Fischer, J., et al. (2013). Intercomparison of shortwave radiative transfer schemes in global aerosol modeling: results from the AeroCom Radiative Transfer Experiment. *Atmospheric Chemistry and Physics*, *13*(5), 2347–2379. https://doi.org/10.5194/acp-13-2347-2013

Raghuraman, S. P., Paynter, D., & Ramaswamy, V. (2019). Quantifying the Drivers of the Clear Sky Greenhouse Effect, 2000–2016. *Journal of Geophysical Research: Atmospheres*, *124*(21), 11354–11371. https://doi.org/10.1029/2019JD031017

Ridley, D. A., Heald, C. L., Ridley, K. J., & Kroll, J. H. (2018). Causes and consequences of decreasing atmospheric organic aerosol in the United States. *Proceedings of the National Academy of Sciences*, *115*(2), 290. https://doi.org/10.1073/pnas.1700387115

Sayer, A. M., Munchak, L. A., Hsu, N. C., Levy, R. C., Bettenhausen, C., & Jeong, M.-J. (2014). MODIS Collection 6 aerosol products: Comparison between Aqua's e-Deep Blue, Dark Target, and "merged" data sets, and usage recommendations. *Journal of Geophysical Research: Atmospheres*, *119*(24), 13,965-13,989. https://doi.org/10.1002/2014JD022453

Shao, Y., Klose, M., & Wyrwoll, K.-H. (2013). Recent global dust trend and connections to climate forcing. *Journal of Geophysical Research: Atmospheres*, *118*(19), 11,107-11,118. https://doi.org/10.1002/jgrd.50836

Sherwood, S. C., Bony, S., Boucher, O., Bretherton, C., Forster, P. M., Gregory, J. M., & Stevens, B. (2015). Adjustments in the Forcing-Feedback Framework for Understanding Climate Change. *Bulletin of the American Meteorological Society*, *96*(2), 217–228. https://doi.org/10.1175/BAMS-D-13-00167.1

Smith, C. J., Kramer, R. J., Myhre, G., Forster, P. M., Soden, B. J., Andrews, T., et al. (2018). Understanding Rapid Adjustments to Diverse Forcing Agents. *Geophysical Research Letters*, *45*(21), 12,023-12,031. https://doi.org/10.1029/2018GL079826

Smith, C. J., Kramer, R. J., Myhre, G., Alterskjær, K., Collins, W., Sima, A., et al. (2020). Effective radiative forcing and adjustments in CMIP6 models. *Atmospheric Chemistry and Physics*, *20*(16), 9591–9618. https://doi.org/10.5194/acp-20-9591-2020

Soden, B. J., Broccoli, A. J., & Hemler, R. S. (2004). On the Use of Cloud Forcing to Estimate Cloud Feedback. *Journal of Climate*, *17*(19), 3661–3665. https://doi.org/10.1175/1520-0442(2004)017<3661:OTUOCF>2.0.CO;2

Soden, B. J., Held, I. M., Colman, R., Shell, K. M., Kiehl, J. T., & Shields, C. A. (2008). Quantifying Climate Feedbacks Using Radiative Kernels. *Journal of Climate*, *21*(14), 3504–3520. https://doi.org/10.1175/2007JCLI2110.1

Soden, B. J., Collins, W. D., & Feldman, D. R. (2018). Reducing uncertainties in climate models. *Science*, *361*(6400), 326–327. https://doi.org/10.1126/science.aau1864

Stier, P., Schutgens, N. A. J., Bellouin, N., Bian, H., Boucher, O., Chin, M., et al. (2013). Host model uncertainties in aerosol radiative forcing estimates: results from the AeroCom Prescribed intercomparison study. *Atmospheric Chemistry and Physics*, *13*(6), 3245–3270. https://doi.org/10.5194/acp-13-3245-2013

Susskind, J., Schmidt, G. A., Lee, J. N., & Iredell, L. (2019). Recent global warming as confirmed by AIRS. *Environmental Research Letters*, *14*(4), 044030. https://doi.org/10.1088/1748-9326/aafd4e

Taylor, K., Ronald, S., & Meehl, G. (2011). An overview of CMIP5 and the Experiment Design. *Bulletin of the American Meteorological Society*, *93*, 485–498. https://doi.org/10.1175/BAMS-D-11-00094.1

Tobin, D. C., Revercomb, H. E., Knuteson, R. O., Lesht, B. M., Strow, L. L., Hannon, S. E., et al. (2006). Atmospheric Radiation Measurement site atmospheric state best estimates for Atmospheric Infrared Sounder temperature and water vapor retrieval validation. *Journal of Geophysical Research: Atmospheres*, *111*(D9). https://doi.org/10.1029/2005JD006103

Thorsen, T. J., Kato, S., Loeb, N. G., & Rose, F. G. (2018). Observation-Based Decomposition of Radiative Perturbations and Radiative Kernels. *Journal of Climate*, *31*(24), 10039–10058. https://doi.org/10.1175/JCLI-D-18-0045.1

Thorsen, T. J., Winker, D. M., & Ferrare, R. A. (2020). Uncertainty in observational estimates of the aerosol direct radiative effect and forcing. *Journal of Climate*, 1–63. https://doi.org/10.1175/JCLI-D-19-1009.1

Trenberth, K. E., Fasullo, J. T., & Balmaseda, M. A. (2014). Earth's Energy Imbalance. *Journal of Climate*, *27*(9), 3129–3144. https://doi.org/10.1175/JCLI-D-13-00294.1

Trenberth, K. E., Zhang, Y., & Fasullo, J. T. (2015). Relationships among top-of-atmosphere radiation and atmospheric state variables in observations and CESM. *Journal of Geophysical Research: Atmospheres*, *120*(19), 10,074-10,090. https://doi.org/10.1002/2015JD023381

Vial, J., Dufresne, J.-L., & Bony, S. (2013). On the interpretation of inter-model spread in CMIP5 climate sensitivity estimates. *Climate Dynamics*, *41*(11), 3339–3362. https://doi.org/10.1007/s00382-013-1725-9

Watson-Parris, D., Bellouin, N., Deaconu, L. T., Schutgens, N. A. J., Yoshioka, M., Regayre, L. A., et al. (2020). Constraining Uncertainty in Aerosol Direct Forcing. *Geophysical Research Letters*, *47*(9), e2020GL087141. https://doi.org/10.1029/2020GL087141

Zhang, B., Kramer, R. J., & Soden, B. J. (2019). Radiative Feedbacks Associated with the Madden–Julian Oscillation. *Journal of Climate*, *32*(20), 7055–7065. https://doi.org/10.1175/JCLI-D-19-0144.1

Zhang, Q., Zheng, Y., Tong, D., Shao, M., Wang, S., Zhang, Y., et al. (2019). Drivers of improved PM2.5 air quality in China from 2013 to 2017. *Proceedings of the National Academy of Sciences*, *116*(49), 24463–24469. https://doi.org/10.1073/pnas.1907956116

Figure 1. Global-mean a) net, b) longwave (LW) and c) shortwave (SW) total radiative flux anomalies from 2003 through 2018 as measured by CERES (black) and the contribution to that total from the sum of radiative responses (red). Respective trendlines are displayed as dashed lines. Uncertainty of +/-2σ is shown for each timeseries, computed as described in the Methods. Linear trends and 95% confidence intervals are provided in text.

Figure 2. Global-mean a) total, b) longwave (LW) and c) shortwave (SW) instantaneous radiative forcing (IRF) estimated from the radiative kernel technique for CERES/AIRS (red) and MERRA-2 (blue). Additional calculations of greenhouse gas-only IRF are also shown using empirical formulas (green) and the SOCRATES radiative transfer model (gray). For reference, the trendline for total radiative flux anomalies (Fig 1a) is displayed with the total IRF as a black dashed line. Uncertainty of +/-2σ is shown with shading for each timeseries, computed as described in the Methods. Linear trends and 95% confidence intervals are provided in text and in Table 1.

Figure 3. Local linear trends from 2003 through 2018 in all-sky shortwave instantaneous radiative forcing (SW IRF) diagnosed in a) CERES/AIRS observations and b) MERRA-2 reanalysis using the radiative kernel differencing technique and c) from direct output of MERRA-2 aerosol IRF. Also, local linear trends over the same time period are shown for aerosol optical depth (AOD) from d) MODIS and e) MERRA-2.

Table 1. Global-mean linear trends (W/m^2/year) and 95% confidence bounds in instantaneous radiative forcing estimated using the radiative kernel differencing technique (first two rows) and MERRA-2 flux diagnostics (third row).

Supplementary Materials for

Observational evidence of increasing global radiative forcing

Ryan J. Kramer[1,2,*], Haozhe He[3], Brian J. Soden[3], Lazaros Oreopoulos[1], Gunnar Myhre[4], Piers M. Forster[5], Christopher J. Smith[5,6]

[1]Earth Sciences Division, NASA Goddard Space Flight Center, Greenbelt, MD 20771, USA
[2]Universities Space Research Association, 7178 Columbia Gateway Drive, Columbia, MD 21046, USA
[3]Rosenstiel School of Marine and Atmospheric Science, University of Miami, 4600 Rickenbacker Causeway, Miami, FL 33149, USA
[4]CICERO Center for International Climate and Environmental Research in Oslo, 0318, Oslo, Norway
[5] School of Earth and Environment, University of Leeds, Leeds, LS2 9JT, UK
[6]International Institute for Applied Systems Analysis (IIASA), Laxenburg, 2351, Austria

Corresponding Author: Ryan J. Kramer (ryan.j.kramer@nasa.gov)

Supplemental Appendix:

SA1. Uncertainty Quantification

Following common practice among previous CERES-focused literature (e.g. Loeb et al. 2018a,b), the trend uncertainty quoted throughout the main text is a measure of the linear regression uncertainty, which is largely driven by the internal variability of the timeseries being analyzed. The 95% confidence intervals are given. It is worthwhile to also evaluate uncertainty due to the various assumptions and diagnostic tools that contribute to the estimate of the IRF. As illustrated by equations 7 and 8 in the main text, all-sky IRF is estimated by subtracting radiative-kernel derived, clear-sky radiative responses from the overall clear-sky TOA radiative imbalance (dR^{CS}). This difference, an estimate of the clear-sky IRF (IRF^{CS}) is then divided by a cloud masking constant, Cl, to convert IRF^{CS} into an all-sky IRF. In this supplementary section, we diagnose uncertainty in IRF trends associated with observations of dR^{CS}, radiative kernels, and Cl. We do so by repeating calculations of the IRF, each time substituting in different values for these terms from different sources as explained below, while keeping all other terms unchanged from the method and data described in the main text. Since the standard trend uncertainty is dependent on these additional sources of uncertainty, it is not practical to combine them to quantify a total, comprehensive measure of uncertainty. We therefore discuss these sources individually, compare their relative magnitude, and summarize the uncertainty budget in Table SA4. We focus on the observational estimate of the IRF.

SA1.1 Uncertainty in dR^{CS}

In this work, observed, total TOA radiative anomalies are diagnosed using radiative flux data from CERES EBAF 4.1. This is identical to CERES EBAF4.0 (Loeb et al. 2018a), except it includes an additional clear-sky radiative flux dataset. While the traditional clear-sky products are comprised only of pixels designated as cloud-free, the new product uses an adjustment factor to mimic a total absence of clouds for all regions, similar to how clear-sky is defined in model simulations (Loeb et al. 2019). While CERES has well documented uncertainty in the magnitude of the TOA radiative flux measurements, our work to estimate the IRF is conducted in anomaly space, where uncertainty in absolute fluxes is irrelevant. Instead, it is the uncertainty due to the stability (or lack thereof) of the observing platform that is important. The presence of spurious trends is frequently assessed by comparing EBAF products to the CERES SSF1deg product, which is considered to be extremely stable (e.g. Loeb et al. 2018a,b). To determine associated uncertainty from stability in the observed timeseries of dR^{CS}, we recompute the IRF using four sources of clear-sky radiative fluxes: CERES EBAF 4.1 assuming clear-skies over the total region, CERES EBAF 4.1 assuming clear-skies over cloud-free regions only (the traditional method), CERES SSF1deg from Terra and CERES SSF1deg from Aqua. All other components of the IRF calculation are consistent across the four estimates. Linear trends of the global-mean IRF are summarized in Table SA1.

CERES clear-sky Source	**Net**	**LW**	**SW**
EBAF 4.1 – clear-sky (for total region)	0.033	0.027	0.0061
EBAF 4.1 – clear-sky (for cloud-free areas of region)	0.026	0.019	0.0064
SSF1deg Terra	0.027	0.026	0.0015
SSF1deg Aqua	0.024	0.025	-0.0004
Standard Deviation	0.0041	0.0035	0.0034

Table SA1. *Linear trends from 2003 through 2018 in global mean net, longwave (LW) and shortwave (SW) all-sky Instantaneous radiative forcing, estimated with differences observational sources of clear-sky radiative fluxes used to diagnose clear-sky TOA radiative flux anomalies. Units are* $W/m^2/yr$.

Across the four estimates, we find a standard deviation of $\sigma = 0.0041$ $W/m^2/yr$ for the Net IRF, $\sigma = 0.0035$ $W/m^2/yr$ in the LW and $\sigma = 0.0034$ $W/m^2/yr$ in the SW. We consider this to be an upper bound on uncertainty associated with the stability of the CERES observations, since stability is not the only source of differences between these datasets. Ultimately, we use the new EBAF 4.1 clear-sky fluxes, representing cloud absence over all regions, in the main analysis since it is more consistent with the way clear-sky is defined in radiative kernels, the additional offline radiative transfer calculations of LW GHG IRF, MERRA-2, and in climate models.

S*A1.2 Radiative kernel uncertainty*

Radiative kernels based on CloudSat/CALIPSO observations are used in this study to quantify radiative responses to changes in temperature, water vapor and surface albedo. Radiative kernels are constant in time (beyond a seasonal cycle) and therefore do not contribute to any spurious trends in the diagnosis of the IRF. However, there is uncertainty in the magnitude of the radiative kernels which can contribute to uncertainty in the anomalies and trend of the

IRF. To quantify this, we estimate the IRF using four different sets of radiative kernels: those based on CloudSat/CALIPSO discussed in the main text, as well as radiative kernels derived from the GFDL (Soden et al. 2008), ECHAM6 (Block and Mauritsen 2013) and HadGEM3 (Smith et al. 2020) climate models. All other components of the calculation are consistent across the four estimates. Linear trends of global-mean IRF are summarized in Table SA2.

Radiative Kernel	**Net**	**LW**	**SW**
CloudSat/CALIPSO	0.0333	0.0272	0.0061
GFDL	0.0313	0.0286	0.0027
ECHAM6	0.0320	0.0297	0.0023
HadGEM3	0.0323	0.0263	0.0060
Standard Deviation	0.0008	0.0015	0.0020

Table SA2. *Linear trends from 2003 through 2018 in global mean net, longwave (LW) and shortwave (SW) all-sky Instantaneous radiative forcing, estimated using different sets of radiative kernels. Units are $W/m^2/yr$.*

We find a standard deviation in trend across the four estimates of $\sigma = 0.0008$ $W/m^2/yr$ for Net IRF, $\sigma = 0.0015$ $W/m^2/yr$ in the LW and $\sigma = 0.0020$ $W/m^2/yr$ in the SW.

SA1.3 Uncertainty in the cloud masking term.

The cloud masking constant, Cl, used to estimate all-sky IRF accounts for the effect of the presence of clouds on the magnitude of the IRF, relative to clear-sky conditions. This quantity is not directly observable and typically requires separate radiative transfer calculations to diagnose. Therefore, like radiative kernels, it contains uncertainty due to radiative transfer error and due to biases in the cloud climatology used in those calculations.

A lack of data prohibits accurately computing the cloud masking directly from observations. All- and clear-sky double-call calculations of the IRF from model simulations offer the best alternative. However, as discussed by Soden et al. (2018), these diagnostics are rarely conducted with model simulations. To the best of our knowledge, none are available for realistic, historical forcing scenarios.

With these limitations, we assume the LW cloud masking is equivalent to the masking of IRF from CO_2 perturbations in this study, which is the dominant GHG driver over the observed period being evaluated. The Coupled Model Intercomparison Project phase 5 (CMIP5, Taylor et al. 2013) includes the necessary double-call calculations from four models to diagnose CO_2 cloud masking, using prescribed sea surface temperature, atmosphere-only simulations where CO_2 concentrations are quadrupled. To diagnose uncertainty in the IRF trends due to Cl, we recompute observed all-sky LW IRF by applying Cl estimated from these four models to the observed clear-sky IRF.

For the SW, there are analogous simulations in CMIP5 (and CMIP6) for aerosol forcing scenarios, but there are no double-call calculations available to diagnose Cl. Instead, we use clear-sky and all-sky Direct Radiative Forcing (DRF) in 15 models included in the AeroCOM Phase II project (Myhre et al. 2013b). Although DRF only includes anthropogenic aerosols, the model-mean Cl from these simulations is 2.70, close to the value from MERRA-2 for SW IRF used in the main text (2.43).

To determine associated uncertainty in IRF trends, we recompute IRF with each LW and SW value of Cl from the model simulations discussed above. Results are summarized in Table SA3.

Model	LW IRF		Model	SW IRF
CanAM4	0.0281		BCC	0.00354
HadGEM2-A	0.0272		CAM4-Oslo	0.00631
INMCM4	0.0253		GEOS_CHEM	0.00627
IPSL-CM5A-LR	0.0243		GISS_MATRIX	0.01081
			GISS-ModelE	0.01024
			GMI	0.00841
			GOCART	0.00913
			HadGEM2	0.00634
			IMPACT-Umich	0.00306
			INCA	0.00726
			ECHAM5-HAM	0.00502
			NCAR-CAM3.5	0.00557
			OsloCTM2	0.00362
			SPRINTARS	0.00290
			TM5	0.00923
Standard Deviation	0.00150		Standard Deviation	0.00253

Table SA3. *Linear trends from 2003 through 2018 in global mean net, longwave (LW) and shortwave (SW) all-sky Instantaneous radiative forcing, estimated using different cloud masking constants derived from 4 CMIP5 models for the LW and 14 AeroCOM models for the SW that provided the radiative flux diagnostics necessary for this calculation.*

The standard deviation across the 4 estimates of LW IRF is $\sigma = 0.00150$ W/m^2/yr and $\sigma = 0.00253$ W/m^2/yr across the 14 estimates of SW IRF. Since different models are used for the LW and SW component, we estimate the standard deviation of the net IRF ($\sigma = 0.00294$ W/m^2/yr), by summing every possible pair of LW and SW IRF trends listed in Table SA3.

SA1.4 Summary

Table SA4 summarizes the results above and additionally shows the trends and 95% confidence intervals for global-mean IRF as outlined in the main text. The 95% confidence intervals represent roughly ±2 standard errors around the mean. To make the additional measures of uncertainty comparable, the values shown in Table SA4 are doubled from the standard deviations outlined in Tables SA1-3 and are divided by the square root of the number of samples that contributed to each uncertainty calculation (to represent of ± 2 standard errors around the mean)

IRF	Trend	95% Confidence Interval (±)	dR^{CS} uncertainty	Radiative kernel uncertainty	Cloud Mask Uncertainty
Net	0.033	0.007	0.004	0.001	0.0015
LW	0.027	0.006	0.0035	0.0015	0.0015
SW	0.006	0.003	0.0035	0.002	0.0018

Table SA4. *Linear trends and 95% confidence intervals (± value) for observed, global-mean net, longwave (LW) and shortwave (SW) Instantaneous Radiative Forcing diagnosed using the methods and data described in the main text as well as uncertainty (±2 standard errors) from clear-sky TOA radiative anomalies (dR^{CS}), radiative kernels and the cloud masking constant.*

All uncertainties are an order of magnitude smaller than the Net and LW IRF trend and of similar magnitude to the trend in the SW. The IRF trends never cross the zero $W/m^2/yr$ threshold given the sources of uncertainty presented. Therefore, the trends are significantly positive. The largest source of uncertainty is in the linear regression itself, represented by the 95% confidence intervals, followed by uncertainty in dR^{CS}. For the Net IRF, this is arguably to be expected, since the trend from the radiative kernel-derived radiative responses is insignificant.

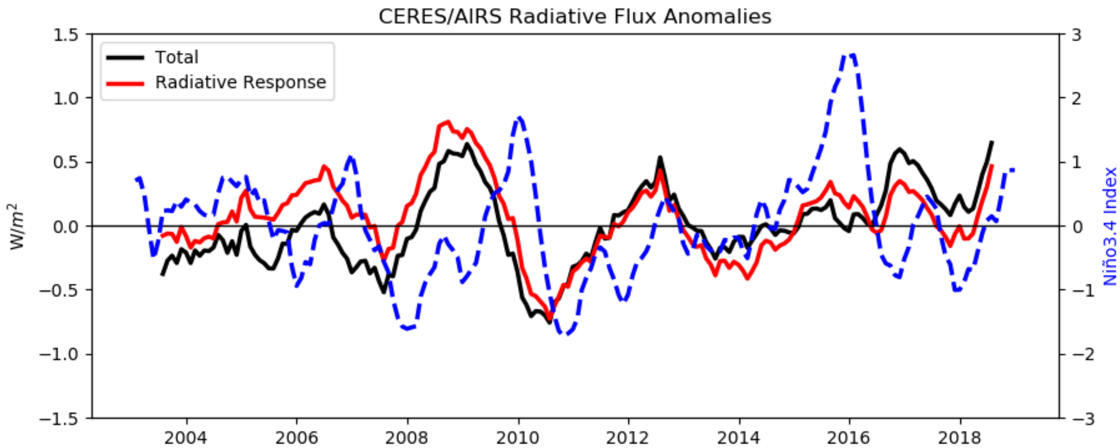

Figure S1. Global-mean total radiative flux anomalies (black) as measured by CERES and the contribution from radiative feedback processes (red). Both quantities are smoothed with a 12-month moving average. The Niño3.4 Index (NOAA/NCEP CPC) is overlaid (blue dashed).

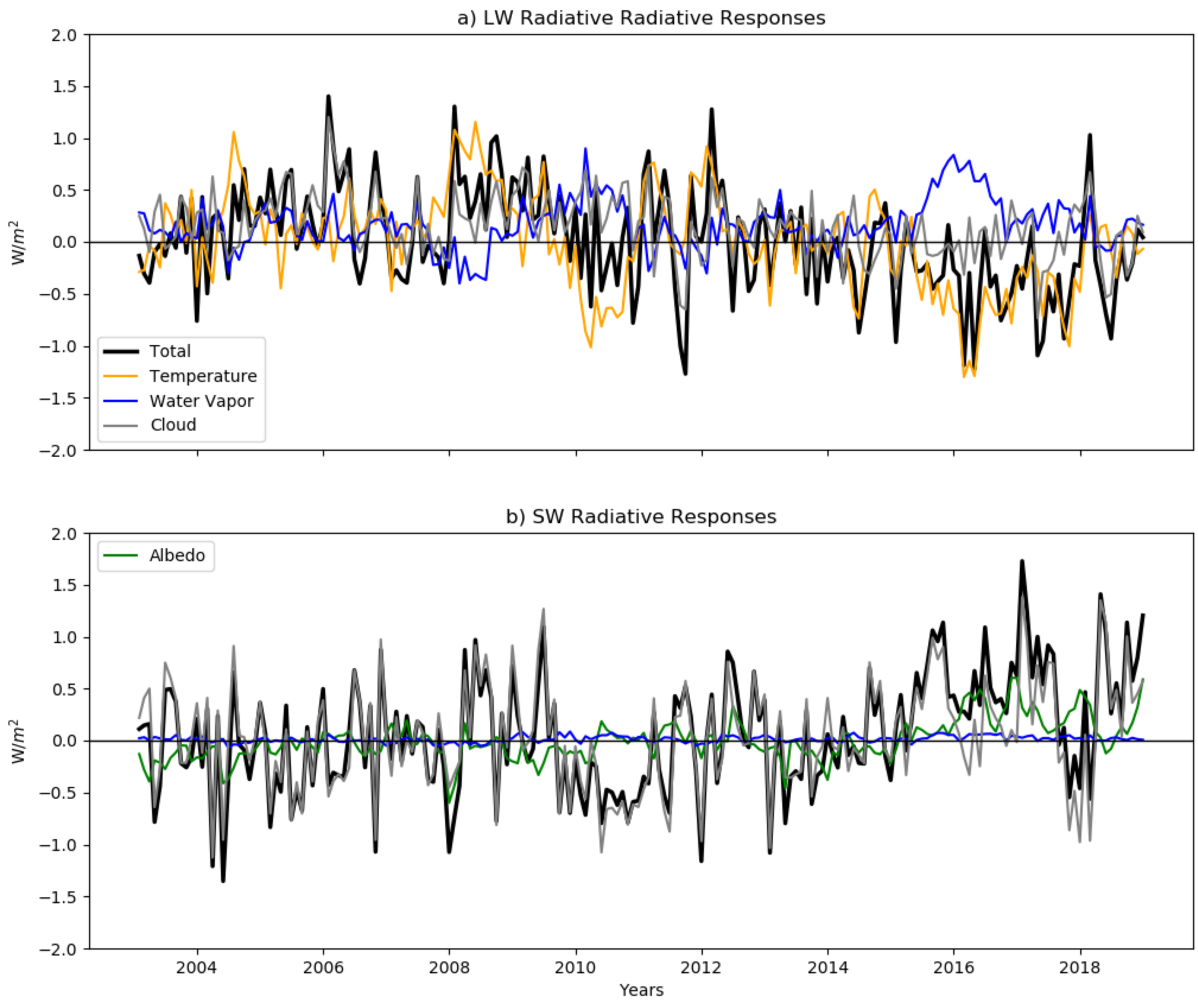

Figure S2. The total a) longwave (LW) and b) shortwave (SW) radiative response and its decomposition into individual radiative responses in CERES/AIRS observations.

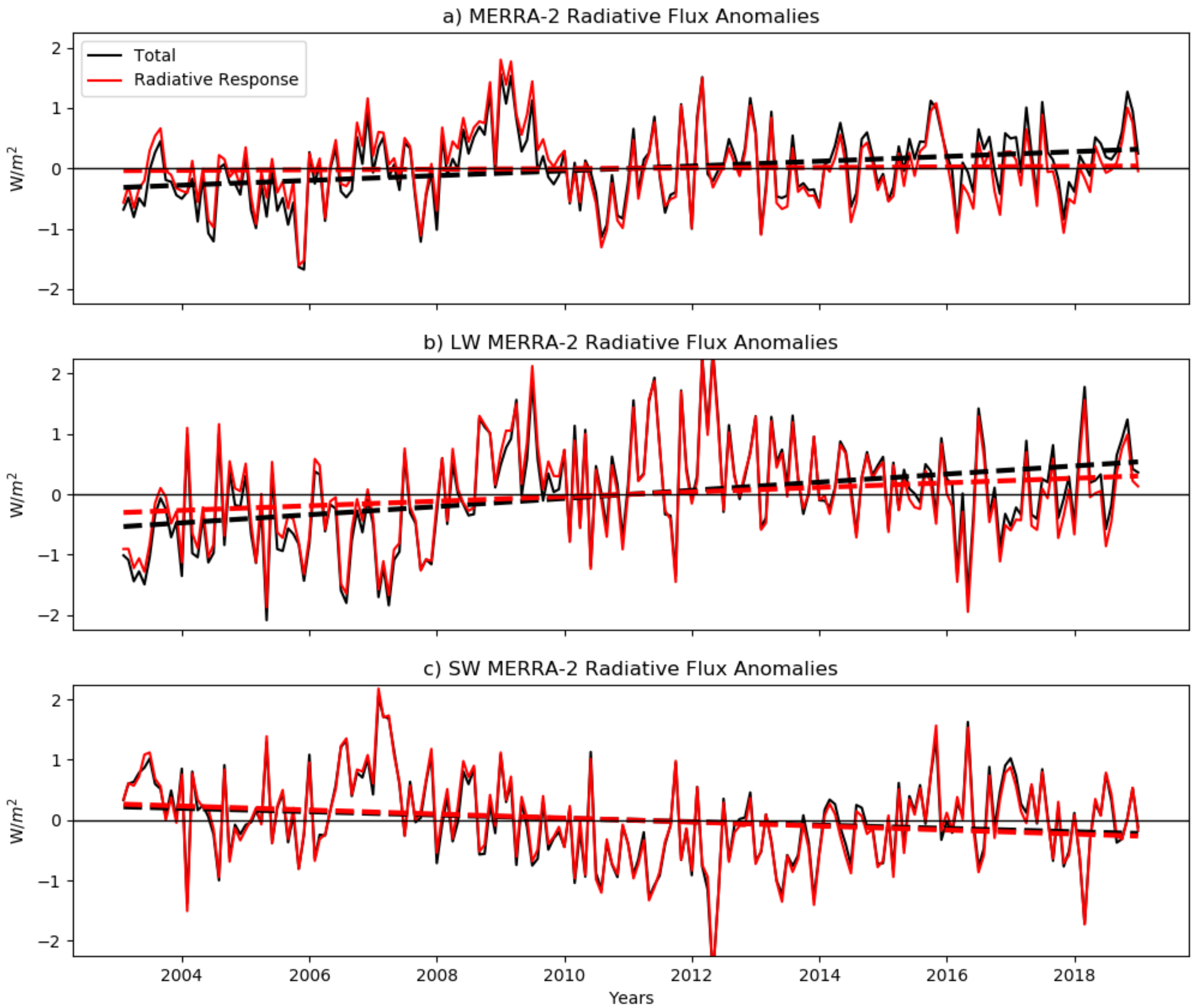

Figure S3. Global-mean, MERRA-2 a) net, b) longwave (LW) and c) shortwave (SW) total radiative flux anomalies (black) from 2003 through 2018 and the contribution to that total from the sum of radiative responses (red). Respective trendlines are displayed as dashed lines.

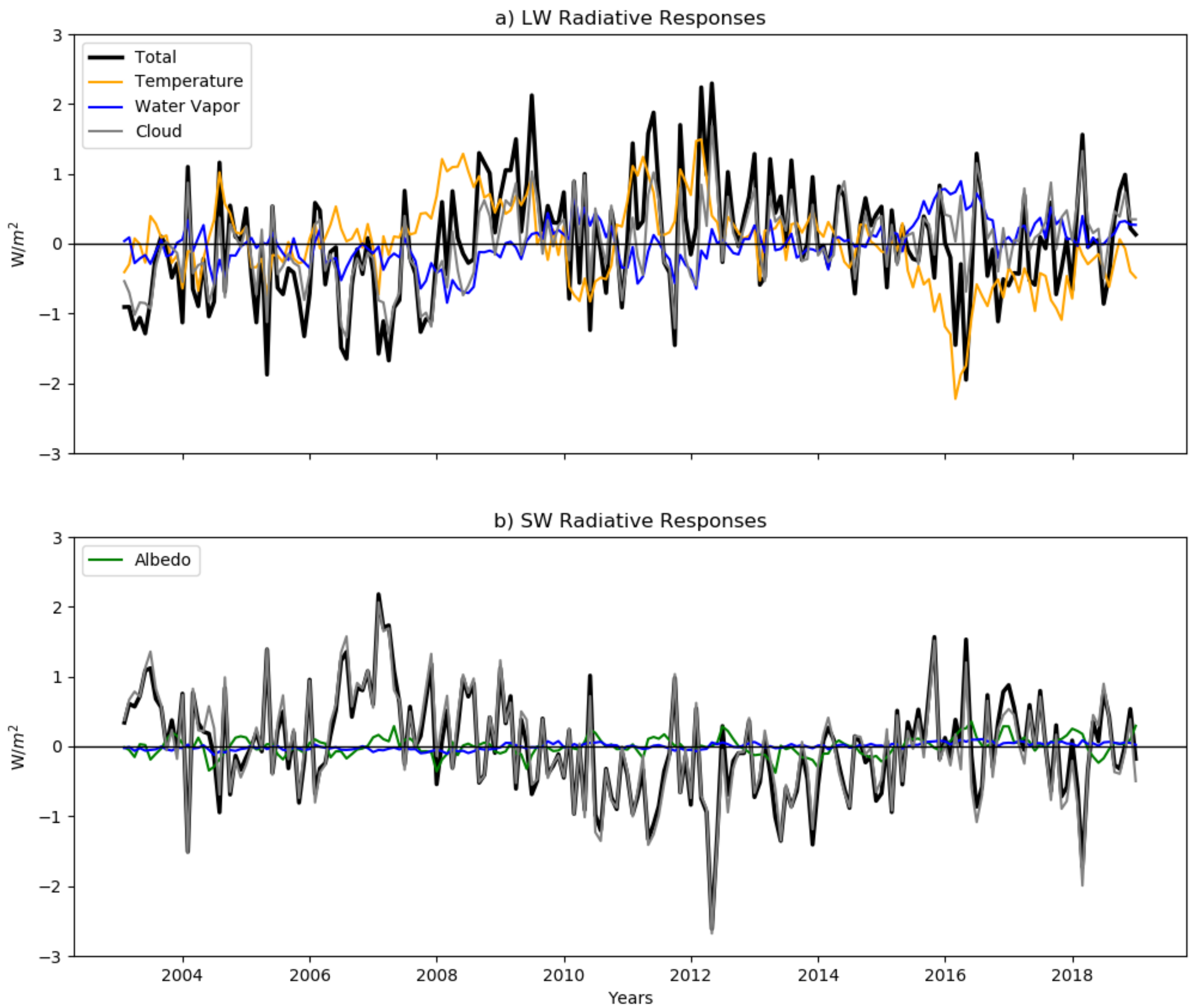

Figure S2. Same as Figure S2 but for MERRA-2.

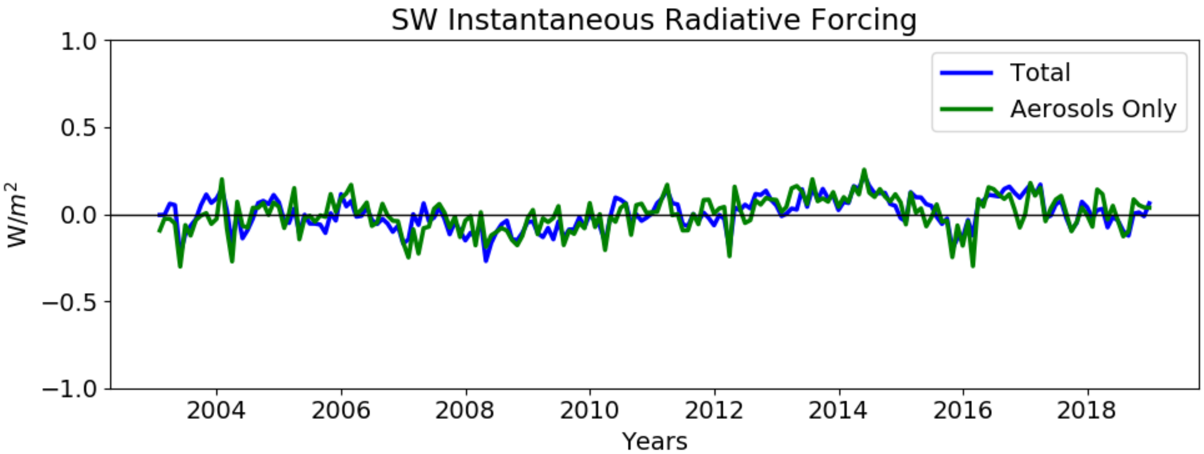

Figure S5. Global-mean a) total shortwave instantaneous radiative forcing (SW IRF) from MERRA-2 derived from the kernel differencing technique and b) aerosol-only SW IRF from direct output of MERRA-2 radiative flux diagnostics.

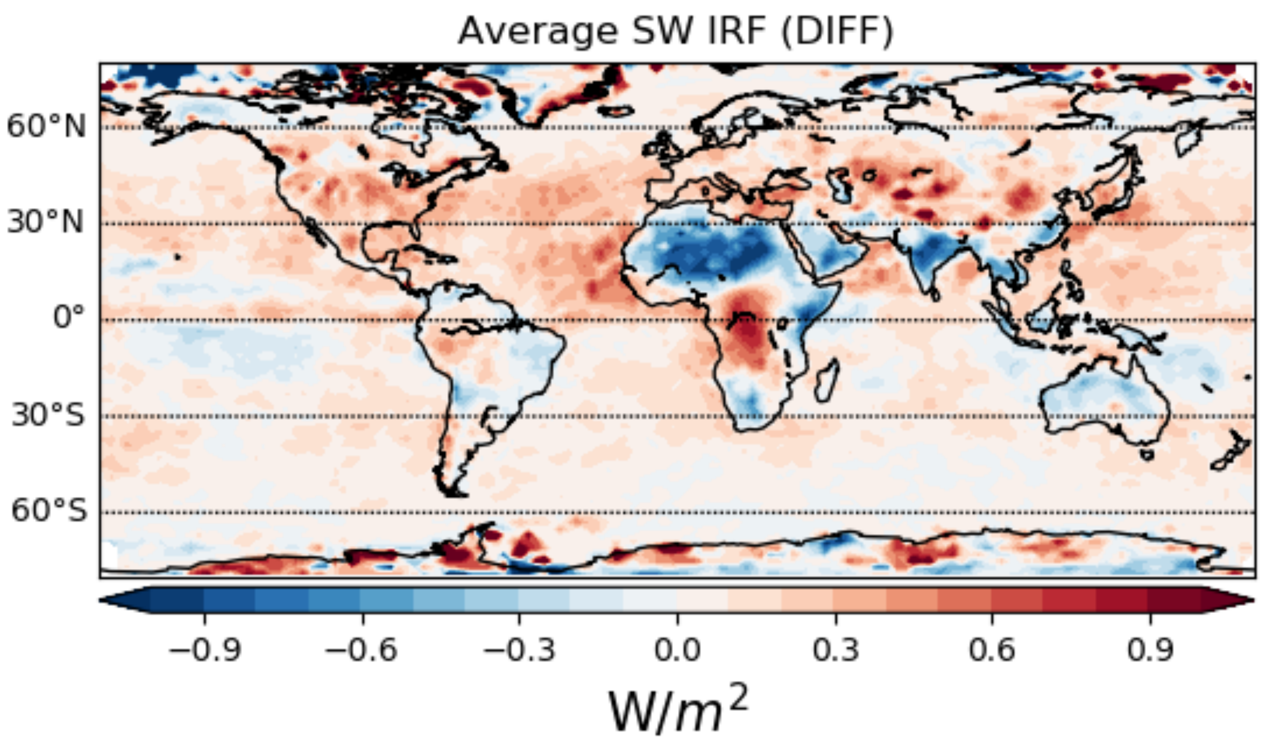

Figure S6. Average difference (CERES/AIRS minus MERRA-2) in SW IRF from 2016 through 2018.

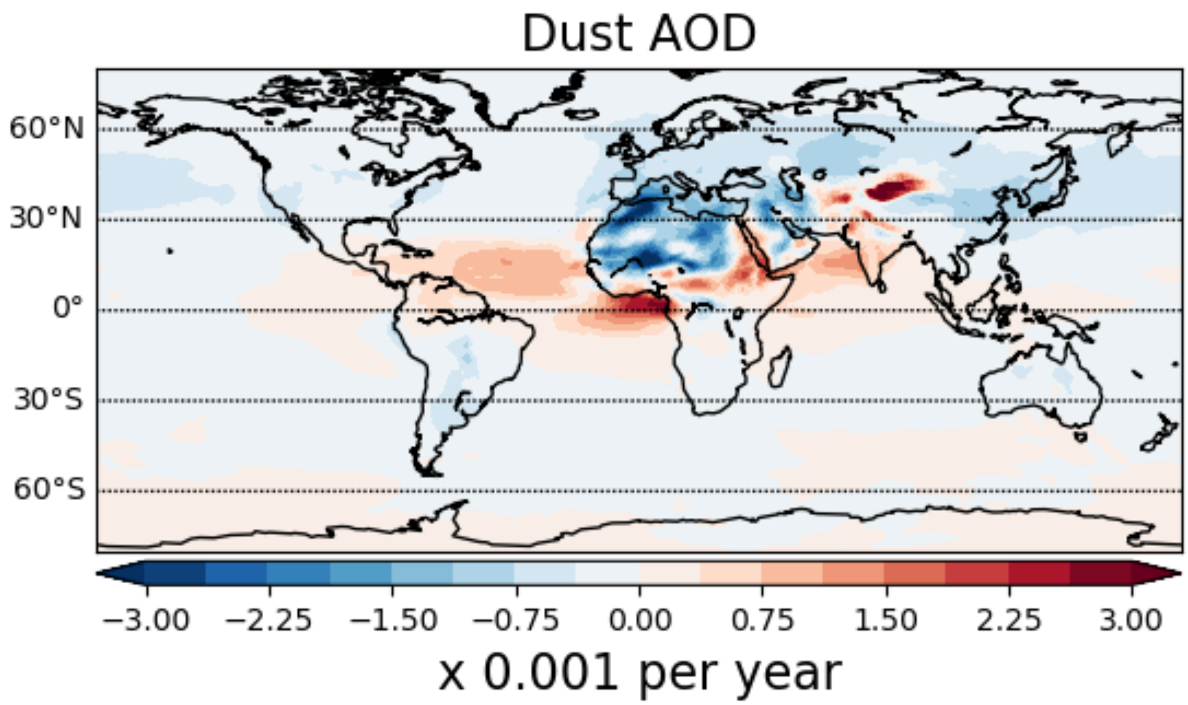

Figure S7. Local linear trends from 2003 through 2018 in dust aerosol optical depth from MERRA-2 reanalysis.

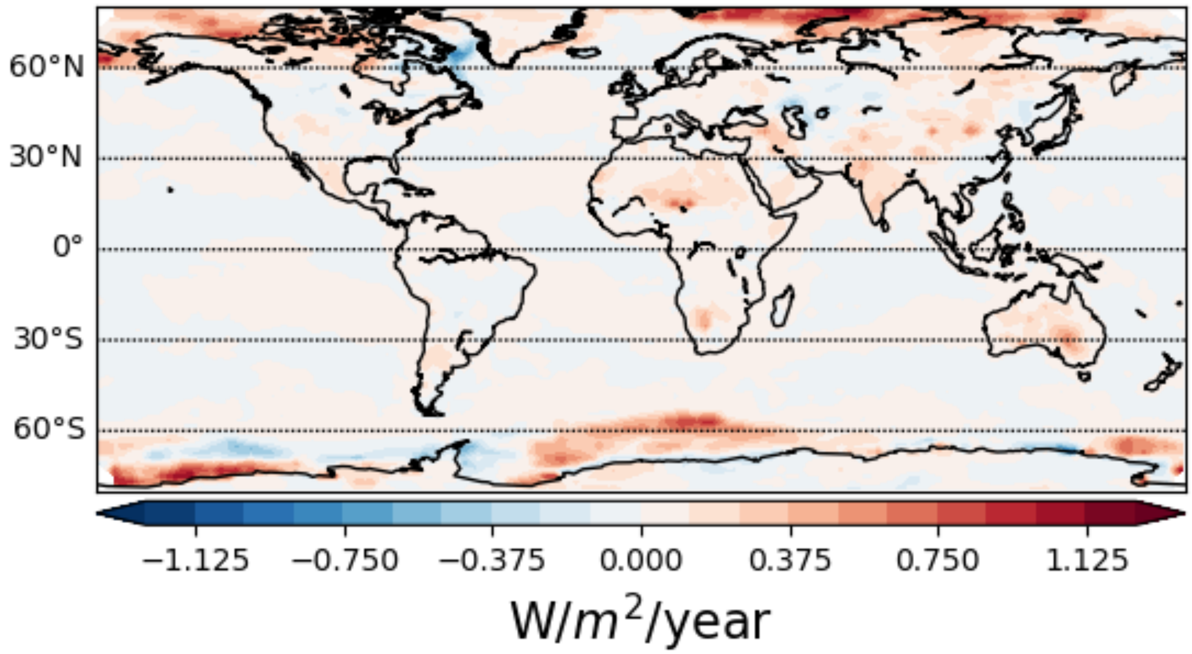

Figure S8. Local linear trends from 2003 through 2018 in clear-sky surface albedo radiative response, used in the kernel differencing method to derive shortwave instantaneous radiative forcing (SW IRF).

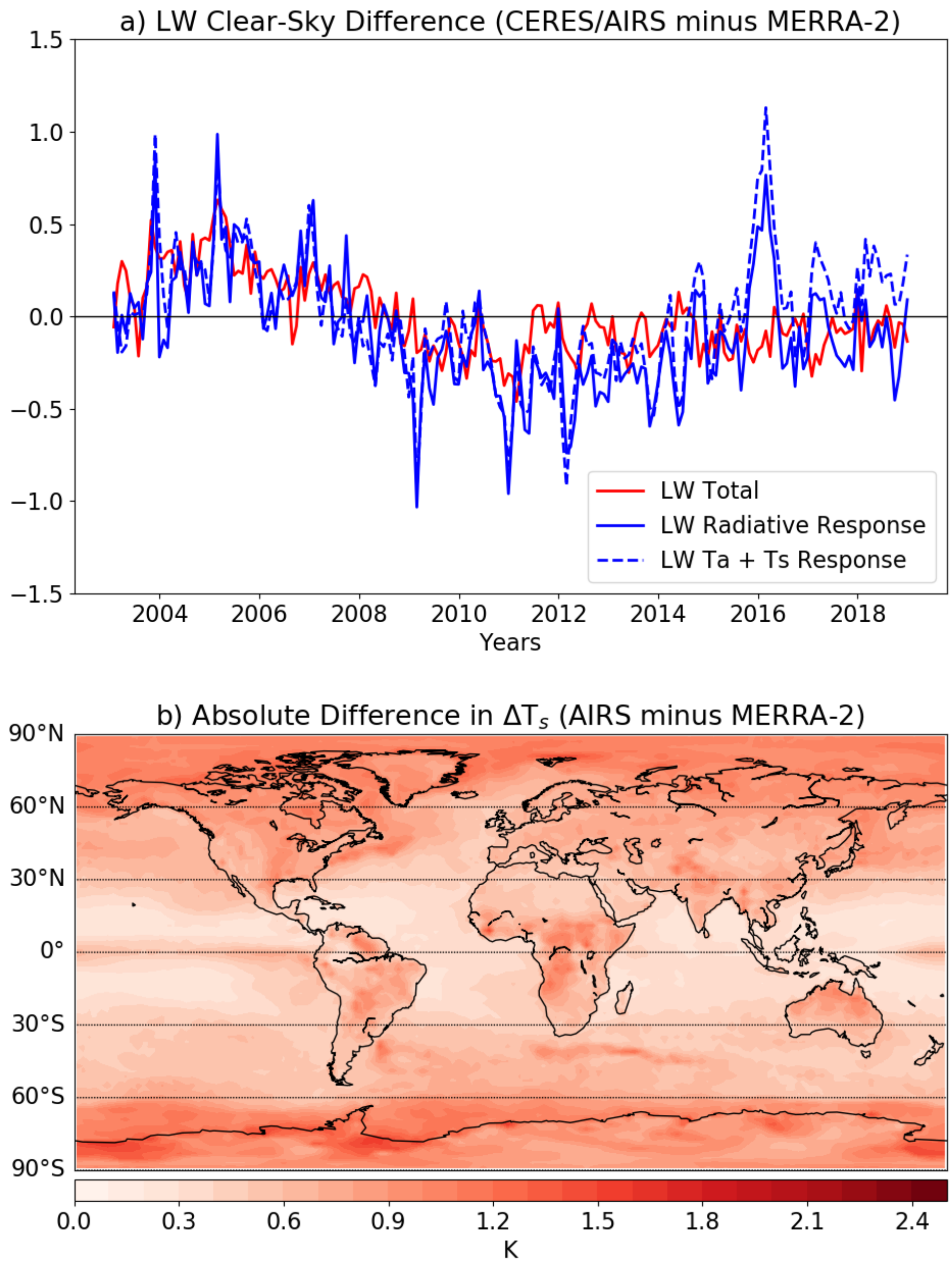

Figure S9. a) Difference between satellite observations and MERRA-2 in global-mean longwave (LW) total radiative flux anomalies (red solid line) as well as the contributions from the sum of LW radiative responses (blue solid) and the LW temperature radiative response (blue dashed), in isolation. b) Mean absolute difference between satellite observations and MERRA-2 in local surface temperature anomalies.

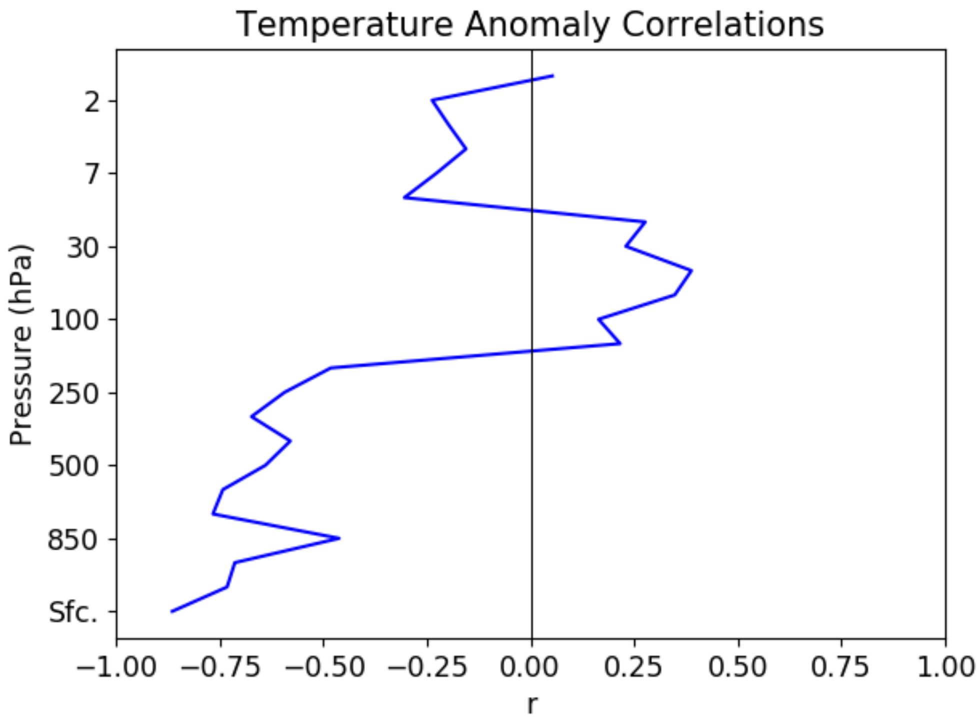

Figure S10. Correlation of the global-mean differences in the temperature feedback between CERES/AIRS and MERRA-2 with differences in temperature anomalies at each vertical level and the surface.

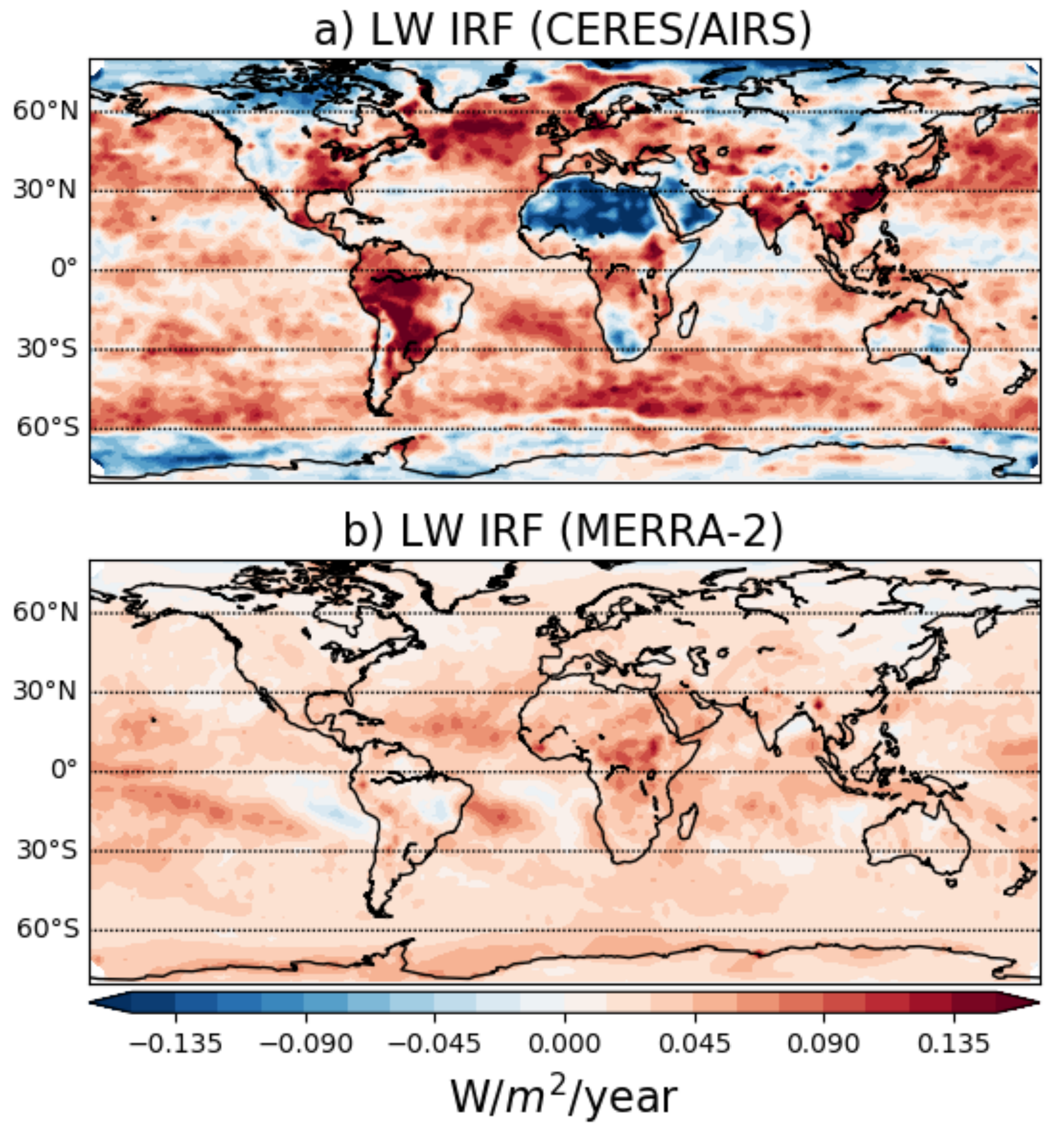

Figure S11. Local linear trends from 2003 through 2018 in all-sky longwave instantaneous radiative forcing (LW IRF) diagnosed in a) CERES/AIRS observations and b) MERRA-2 reanalysis.